NOVA SCHOOL OF
SCIENCE & TECHNOLOGY

DEPARTAMENT OF
LIFE SCIENCES

André Miguel Forte Meireis

BSc in Cellular and Molecular Biology

LYSOSOMAL TARGETING AND PHOTOTHERMAL EFFECT OF ANTIBOFY FUNCTIONALIZED GOLD NANOPARTICLES IN COLORECTAL CANCER CELLS

MASTER IN MOLECULAR GENETICS AND BIOMEDICINE

NOVA University Lisbon

September, 2022

DEPARTAMENT OF LIFE SCIENCES

LYSOSOMAL TARGETING AND PHOTOTHERMAL EFFECT OF ANTIBOFY FUNCTIONALIZED GOLD NANOPARTICLES IN COLORECTAL CANCER CELLS

ANDRÉ MIGUEL FORTE MEIREIS

BSc in Cellular and Molecular Biology

Adviser: Pedro Miguel Ribeiro Viana Baptista
Full Professor, NOVA school of Science and Technology

Co-advisers: Maria Alexandra Núncio de Carvalho Ramos Fernandes
Assistant Professor with habilitation, *NOVA school of Science and Technology*

Examination Committee:

Chair: Doctor Pedro Manuel Brõa Costa, Assistant Professor, NOVA school of Science and Technology

Rapporteurs: Doctor José Ricardo Ramos Franco Tavares, Assistant Professor with habilitation, NOVA school of Science and Technology

Adviser: Doctor Pedro Miguel Ribeiro Viana Baptista, Full Professor, NOVA school of Science and Technology

MASTER IN MOLECULAR GENETICS AND BIOMEDICINE

NOVA University Lisbon
September, 2022

Lysosomal targeting and photothermal effect of antibody functionalized gold nanoparticles in colorectal cancer cells

This document was created with Microsoft Word text processor and the NOVAthesis Word template.

ACKNOWLEDGMENTS

Firstly, I would like to thank my supervisor Professor Pedro Baptista for the continued guidance throughout the whole year, for all the talks we had science related and unrelated. For his method of teaching us to "to fish" rather than "fishing" for us, which I feel that made me grow as person and has a scientist way beyond my expectations. To Professor Alexandra Fernandes for the continued support and patience throughout the whole year. Both have taught me a lot in this short period of time and for that I give you my utmost thanks.

Huge thanks to Susana, the best lab mate I could have asked for, to Beatriz and Maria that I got to know better in the past year. For our many talks in our very quick lunch breaks and our many laughs in the lab.

Special thanks to my seniors, Sandra, Daniela, Margarida, André, Ruben, and Catarina for teaching me the ropes in the lab and for their continued support in this last year. They were people I could rely on whenever I needed anything.

To my great friends who I could always share a good laugh with in all these years and whom I have so many great memories with.

To my lovely family, my mother, father, sister and to my grandparents that have always been there for me, motivating me to always strive for more and that made me the man I am today.

This work is financed by national funds from FCT - Fundação para a Ciência e a Tecnologia, I.P., in the scope of the project 2022.04315.PTDC, and to projects UIDP/04378/2020 and UIDB/04378/2020 of the Research Unit on Applied Molecular Biosciences - UCIBIO and the project LA/P/0140/2020 of the Associate Laboratory Institute for Health and Bioeconomy - i4HB.

“To raise new questions, new possibilities, to regard old problems from a new angle, requires creative imagination and marks a real advance in science.”

Albert Einstein .

ABSTRACT

Cancer is on the verge of becoming the number one cause of deaths worldwide, despite all the efforts and numerous studies regarding the molecular mechanisms underlying carcinogenesis and the development of new approaches to cancer therapy. Current therapies still have major downsides and to overcome them it is of high importance to develop novel approaches that offer better selectivity, minimizing the death of healthy cells, and that are able to overcome the resistance of cancer cells.

Autophagy is one of the main cellular mechanisms used by cancer cells to produce enough energy for tumor development and to also resist the effects from certain therapeutic drugs. This mechanism is extremely reliant on the lysosomes and if these were to be disrupted so would the mechanism. In this work we report the study of antibody functionalized gold nanoparticles as potential photothermal agents for specific photoirradiation of the lysosomes in cancer cells.

Antibody functionalized gold nanoparticles for specific targeting of the lysosomal membrane were synthesized, and cellular uptake and phothotermia assays were performed in a colorectal cancer cell line. Cellular uptake assays revealed increased particle uptake and lysosomal accumulation of antibody functionalized gold nanoparticles whilst cell viability studies regarding photothermia assays showed no effect on cellular viability. Results demonstrated the active targeting of lysosomes by the synthesized nanoparticles, validating their potential as targeting agents. Future work is needed to evaluate the potential of these particles as possible photothermal agents.

Keywords: Cancer; Autophagy; Gold Nanoparticles; Cellular Uptake; Lysosomes; Photothermia

RESUMO

O cancro está prestes a tornar-se a causa número um de mortes em todo o mundo, apesar de todos os esforços e inúmeros estudos sobre os mecanismos moleculares subjacentes à carcinogénese e o desenvolvimento de novas abordagens para a terapia do cancro. As terapias atuais ainda apresentam grandes desvantagens e para superá-las é de grande importância desenvolver novas abordagens que ofereçam melhor seletividade, minimizando a morte de células saudáveis, e que sejam capazes de superar a resistência das células cancerígenas.

A autofagia é um dos principais mecanismos celulares utilizados pelas células cancerígenas para produzir energia suficiente para o desenvolvimento do tumor e para resistir aos efeitos de certas drogas terapêuticas. Este mecanismo é extremamente dependente dos lisossomas e, se estes fossem rompidos, o funcionamento deste mecanismo seria afetado. Neste trabalho relatamos o estudo de nanopartículas de ouro funcionalizadas com anticorpos como potenciais agentes foto-térmicos para foto-irradiação específica dos lisossomas em células cancerígenas.

Foram sintetizadas nanopartículas de ouro funcionalizadas com anticorpos para um direcionamento específico da membrana dos lisossomas e foram realizados ensaios de captação celular e foto-termia numa linha celular de cancro colorretal. Os ensaios de captação celular revelaram um aumento da captação das nanopartículas de ouro funcionalizadas com anticorpo e uma acumulação nos lisossomas, enquanto os estudos de viabilidade celular em relação aos ensaios de foto-termia não demonstraram nenhum efeito na viabilidade celular. Os resultados demonstraram uma acumulação preferencial das nanopartículas nos lisossomas, validando a sua capacidade de reconhecimento dos lisossomas. Trabalhos futuros são necessários para avaliar o potencial destas partículas como possíveis agentes foto-térmicos.

Palavas chave: Cancro; Autofagia; Nanopartículas de Ouro; Captação Celular; Lisossomas; Foto-termia

CONTENTS

Acknowledgments ix
Abstract xiii
Resumo xv
List of Figures xxi
List of Tables xxiv
List of Abbreviations xxvii
1 INTRODUCTION 1
  1.1 Cancer 1
    1.1.1 Cancer Statistics 1
    1.1.2 Cancer Development 2
    1.1.3 Colorectal cancer 4
  1.2 The role of Lysosomes in Cancer Cell Survival 5
    1.2.1 Autophagy 6
    1.2.2 Autophagy in cancer 7
  1.3 Cancer therapies 9
    1.3.1 Nanotechnology and the Rise of Nanomedicine 9
    1.3.2 Nanoparticles in drug delivery and targeting 10
    1.3.3 Cellular uptake of Nanoparticles 11
    1.3.4 Gold Nanoparticles 12
  1.4 Photothermal Therapy in cancer therapy 13
  1.5 Context and objectives 14

2 MATERIALS AND METHODS 17
2.1 Synthesis of citrate capped gold nanoparticles 17
2.2 Citrate capped AuNP functionalization with PEG-COOH 18
2.2.1 AuNP Pegylation 18
2.2.2 Ellman´s Assay 19
2.3 AuNP@PEG-COOH functionalization with Anti-LAMP2A 19
2.3.1 Functionalization with the Antibody 20
2.3.2 Bradford Assay 21
2.4 Gold nanoparticle characterization 21
2.4.1 AuNP characterization by UV-Visible Spectrophotometry 21
2.4.2 DLS and Zeta Potential 22
2.5 Cell Culture 22
2.5.1 Cell culture maintenance 23
2.6 Cell Challenge with Gold Nanoparticles 23
2.6.1 Assessment of AuNP uptake through U.V-visible spectrophotometry 24
2.6.2 Fractionating of Challenged Cells 24
2.6.3 ICP-AES 25
2.7 Assessment of Cell Viability 25
2.7.1 MTS Assay 25
2.7.2 Trypan Blue Exclusion Method 26
2.8 Western Blot 26
2.8.1 Pierce Assay 26
2.8.2 Sample Preparation 27
2.8.3 SDS-PAGE Gel Electrophoresis and nitrocellulose membrane transfer 27
2.8.4 Membrane Blocking and Antibody Staining 28
2.8.5 Film exposure 29
2.8.6 Membrane Stripping 29

2.8.7 β-Actin control 29

2.9 Immunofluorescence Microscopy 29

2.10 Photothermy Assay 31

3 RESULTS AND DISCUSSION 33

3.1 Characterization of synthesized AuNPs 33

3.1.1 Characterization of Citrate Capped AuNPs 33

3.1.2 Characterization of AuNP@PEG-COOH 34

3.1.3 Characterization of AuNP@PEG-COOH@Anti-LAMP2A 35

3.2 Challenging of cells with Au-nanoconjugates 37

3.2.1 Uptake of Gold Nanoparticles 37

3.2.2 Intracellular accumulation of Gold Nanoparticles 38

3.2.3 Lysosome presence in the cellular fractions 39

3.3 Immunofluorescence Microscopy 42

3.4 Photothermy 44

4 CONCLUSIONS AND FUTURE PERSPECTIVES 49

References 51

Annexes 57

Annex A 57

Annex B 61

LIST OF FIGURES

Figure 1.1- *Number of new cancer cases detected and cancer related deaths in 2020 worldwide for both sexes and all ages.* 1

Figure 1.2- *Number of new cancer cases detected and cancer related deaths in 2020 for both sexes and all ages in Portugal.* 2

Figure 1.3- *The six core hallmarks of cancer and the recently studied emerging hallmarks and enabling factors.* 4

Figure 1.4- *Representation of the Autophagy process.* 7

Figure 1.5- *The dual and contradictory roles of autophagy in cancer.* 8

Figure 1.6- *Nanoparticle drug delivery system targeting mechanisms.* 11

Figure 1.7- *Nanoparticle cellular internalization pathways.* 12

Figure 2.1- *Representation of citrate capped gold nanoparticle (AuNP) functionalization with polyethylene glycol harboring a carboxylic acid functional group (SH-EG(8)-COOH) (PEG-COOH).* 18

Figure 2.2- *Representation of AuNP@PEG-COOH functionalization with Anti-LAMP2A antibody [EPR4207(2)]- Lysosome Marker (ab125068) through EDC/NHS coupling reaction.* 20

Figure 3.1- *Obtained spectra of citrate capped gold nanoparticles (AuNP), PEG-COOH functionalized AuNPs (AuNP@PEG-COOH) and Anti-LAMP2A functionalized AuNP@PEG-COOH (AuNP@PEG-COOH@Anti-LAMP2A).* 36

Figure 3.2- *Work scheme representing the several steps of lab work.* 37

Figure 3.3- *Gold nanoparticle uptake by HCT116 cells after 24 hours of incubation.* 38

Figure 3.4-*Representative images of western blot analysis of membranes stained only with the secondary antibody, Goat Anti-Rabbit IgG H&L (HRP) (ab205718).* 41

Figure 3.5- *Representative images of western blot analysis of membranes stained with the primary antibody, Anti-LAMP2A antibody [EPR4207(2)]- Lysosome Marker (ab125068) and secondary antibody, Goat Anti-Rabbit IgG H&L (HRP) (ab205718)*....................42
Figure 3.6- *Bright field and DAPI, FITC, G2A fluorescent images.*....................44
Figure A1- *Ellman´s Calibration curve.*....................57
Figure A2- *Calculation for maximum surface area coverage of a AuNP@PEG-COOH with an IgG (Anti-LAMP2A antibody [EPR4207(2)]-Lysosome Marker (ab125068))*....................58
Figure A3- *Bradford calibration curve.*....................58
Figure A4- *Calibration curve performed by Heiss et al*....................59
Figure A5- Pierce *calibration curve*....................60
Figure A6- *Semi-dry transfer system representation*....................60
Figure B1- *Representation of the 96 well plate for photothermy*....................61
Figure B2- *Representation of the 96 well plate for Immunofluorescence Microscopy*....................62

LIST OF TABLES

Table 2.1: *SDS-PAGE gel composition* 28

Table 2.2: *Semi-dry transfer system buffer composition* 28

Table 3.1: *Gold nanoparticle characterization through UV-Visible Spectrophotometry, Dynamic Light Scattering and Zeta potential.* 36

Table 3.2: *Gold concentration detected through ICP-AES in cellular fractions.* 39

Table 3.3: Temperature measurements before and after laser irradiation. 45

Table 3.4: *MTS assay.* 46

LIST OF ABBREVIATIONS

APC -Adenomatous polyposis coli
AuNPs- Gold nanoparticles
AuNP@PEG-COOH-Pegylated AuNP
AuNP@PEG-COOH@Anti-LAMP2A- Pegylated AuNP functionalized with Anti-LAMP2A antibody
BSA -Bovine serum albumin
CRC -Colorectal cancer
DAPI- 4′,6-diamidino-2-phenylindole
DDS- Drug Delivery System
DLS- Dynamic light scattering
DMEM -Dulbecco's Modified Eagle Medium
DTNB -5,5′-dithio-bis(2-nitrobenzoic)
EPR- Enhanced permeability and retention
FITC- Fluorescein isothiocyanate
FAP- Familial Adenomatous Polyposis
GFP -Green Fluorescent Protein
HNPCC- Hereditary non-polyposis colorectal cancer
HS-PEG(8)-COOH -Alpha-Thio-omega-(propionic acid) octa (ethylene glycol)
ICP-AES- Inductively coupled plasma atomic emission spectroscopy
LAMP2A- Lysosomal associated membrane protein 2A
LMP- Lysosome Membrane Permeabilization
LSPR- Localized Surface Plasmon Resonance
MTS -3-(4,5-dimethylthiazol-2-yl)-5-(3-carboxymethoxyphenyl)-2-(4-sulfophenyl)-2H-tetrazolium
NIR -Near-infrared light
PEG- Polyethylene glycol
PTT -Photothermal therapy
RT- Room temperature
SDS -Sodium dodecyl sulfate
TRITC- Tetramethylrhodamine isothiocyanante
UV-Vis -Ultraviolet-Visible light

1

INTRODUCTION

1.1 Cancer

1.1.1 Cancer Statistics

Cancer has always been a major public health problem all around and is now on the verge of becoming the leading cause of deaths worldwide[1,2]. According to recent data from the World Health Organization[3] (**Figure 1.1**), 19 million new cancer cases were detected, and 10 million cancer related deaths reported worldwide in 2020. Breast, lung, and colorectal cancer rank top three in the number of new cases in 2020 with, 2.3 million (11.7%), 2.2 million (11.4%) and 1.4 million (7.3%) diagnosed cases respectively and lung, colorectal and liver cancers ranking top three in cancer related deaths with 1.8 million (18%), 935 173 (9.4%) and 830 180 (8.3%) reported deaths respectively.

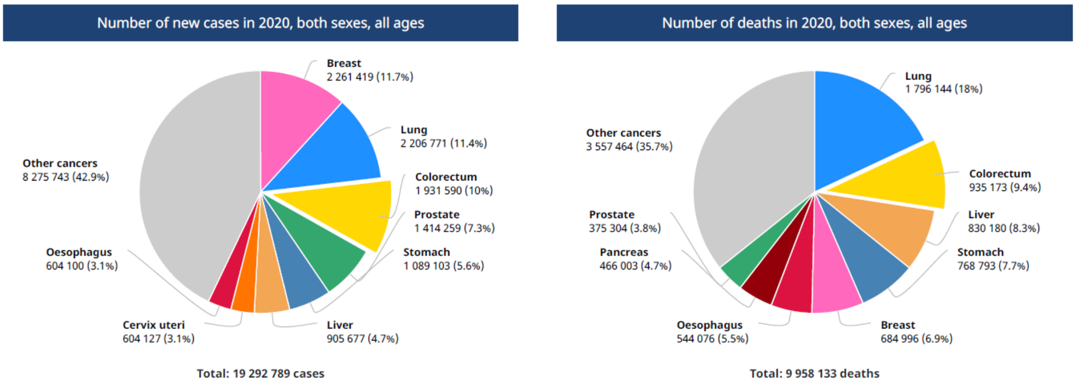

Figure 1.1- *Number of new cancer cases detected and cancer related deaths in 2020 worldwide for both sexes and all ages. Adapted from* [3]

In Portugal, colorectal, breast and prostate cancers were the most frequent with 10 501 (17.4%), 7 041 (11.6%), 6 759 (11.2%) diagnosed cases in 2020 and lung, colorectal and stomach cancers responsible for the most deaths with 4 797 (15.9%), 4 320 (14.3%) and 2 332 (7.7%) reported deaths in 2020 (**Figure 1.2**).

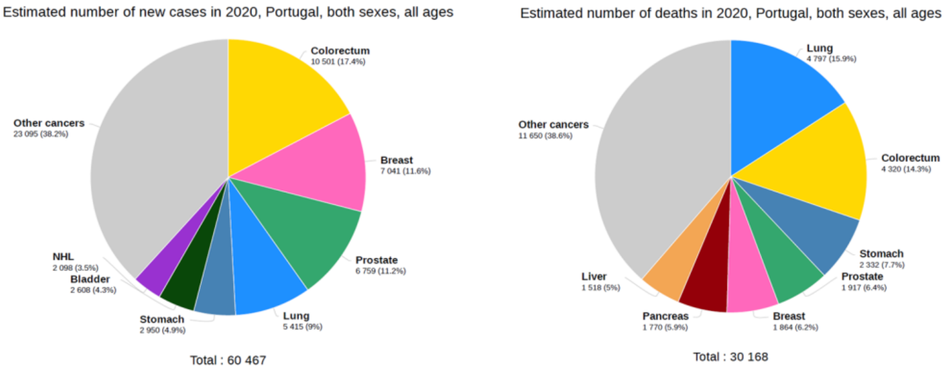

Figure 1.2- ***Number of new cancer cases detected and cancer related deaths in 2020 for both sexes and all ages in Portugal.*** *Data obtained through https://gco.iarc.fr/*

In the last couple of decades, currently employed cancer therapies such as surgery, radiotherapy and chemotherapy have been thoroughly studied and their efficiency improved through a more selective targeting of cancer cells, minimizing the death of healthy cells, and overcoming tumor therapy resistance. Furthermore, the combination of these therapies, combined cancer therapy, has achieved remarkable results with an incredible improvement in cancer survival rates. However in recent years, as a result of the growing knowledge regarding the complex molecular changes that accompany the development and resilience of cancer cells, promising molecular approaches have surfaced to assist in the fight against cancer. [4,5]

1.1.2 Cancer Development

Cancer is characterized as the abnormal growth of cells, due to the bypass of cell cycle control mechanisms, because of acquired mutations in tumor suppressor genes and proto-oncogenes disrupting the precise control exerted by several cellular mechanisms, including cell division, differentiation, and cell death. Tumor suppressor genes, such as *Retinoblastoma 1 (RB1)* and *P53,* play an important role in suppressing cancer development through the regulation of cell growth and differentiation in normal cells. Mutations in tumor suppressor genes can lead to a lack of expression or inactivation of these genes, causing a deregulation in cell growth and development. Proto-oncogenes play a key role in several biological processes of normal cell proliferation and differentiation, by stimulating cell division, and inhibiting cell differentiation and programmed cell death (apoptosis). Oncogenes are generated by mutations in proto-oncogenes and are usually in an overexpressed stated, overstimulating cell proliferation whilst completely inhibiting cell differentiation and apoptosis. As such an abnormal activation of oncogenes accompanied by an inactivation of tumor-suppressor genes gives rise to the development of cancer cells. [6–9]

As they begin to develop, cancer cells acquire distinctive traits that allow tumor growth, survivability and metastatic proliferation, commonly referred to as the hallmarks of cancer as represented in **Figure 1.3**.[6,10] In the year 2000, with knowledge gathered through the study of cancer, six hallmarks were defined, classifying the distinctive behavior of cancer cells at a molecular level[11]. In 2011 with the advances in cancer research two emerging hallmarks, the deregulation of cell metabolism and the ability to avoid the immune system were also identified along with the first two enabling characteristics responsible for the acquisition of the previous hallmarks, cancer's genomic instability and tumor promoting inflammation[6]. Besides the aforementioned enabling characteristics and hallmarks of cancer, new enabling characteristics and hallmarks are being proposed such as, the ability to unlock phenotypic plasticity where cancer cells originating from a well differentiated cell type can dedifferentiate back to progenitor like cell states becoming unbound of the antiproliferative state of differentiated cells[12,13]and inhibiting the return to such state, non-mutational epigenetic reprograming[14], the effect of polymorphic microbiome variability in cancer phenotypes[15,16] and the stimulation of tumor development and malignancy progression caused by the presence of senescent cells[17].

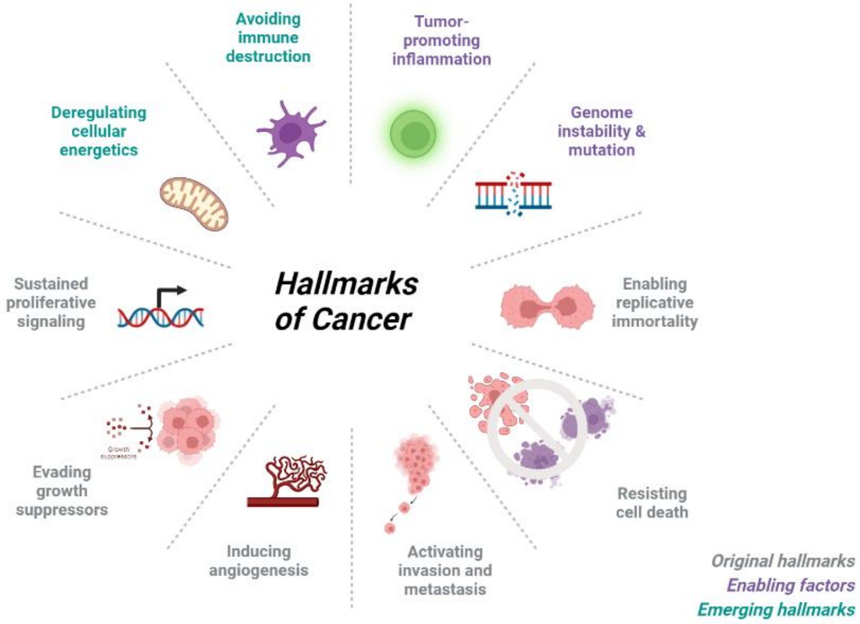

Figure 1.3- *The six core hallmarks of cancer and the recently studied emerging hallmarks and enabling factors. The acquisition of these hallmarks, through the several known enabling characteristics such as, the instability of the genome that gives rise to dozens of new mutations in cancer cells, are of the utmost importance to ensure the growth and proliferation of cancer cells, allowing their uncontrolled growth by sustaining proliferative signaling whilst evading growth suppressors. Generating enough energy through the reprograming of the cellular metabolism and gathering enough nutrients through the access of blood vessels by inducing the growth of new vessels or accessing existing ones which will also in turn allow for cancer cell invasion and metastasis. Ensuring their survival through the avoidance of the immune system, resistance of cell death and the enabling of replicative immortality evading a state of senescence.* [6] *Created with Biorender.com.*

1.1.3 Colorectal cancer

Colorectal cancer (CRC) is the third most commonly diagnosed cancer worldwide and ranks second regarding cancer related deaths.[3] CRC is characterized by an abnormal growth of cells leading to the formation of malignant solid tumors in the final part of the gastrointestinal system encompassing the colon and the rectum.

As is the case for most cancers, CRC is caused by mutations targeting oncogenes leading to an increase in function or to the acquisition of novel functions, tumor suppressor genes leading to a loss of function, and mutations on DNA repair mechanisms causing an increase in the number of mutations. [18,19] These mutations can be caused by a variety of genomic instabilities such as chromosomal instability, DNA mismatch repair defects, CpG island methylator phenotype, base-excision repair defects, and microsatellite instability.[18,20]

Colorectal carcinomas can be classified as sporadic, inherited, and familial according to the origin of the mutation. Sporadic cancers account for about 70% of all colorectal cancers and originate from point mutations that appear during life affecting only individual cells and are unrelated with inherited syndromes. Generally, in sporadic cancers, the molecular pathogenesis is quite heterogeneous as different genes are the targets for mutations. On the other hand, in 70% of all CRC cases, pathogenesis follows a specific onset and succession of mutations starting with the formation of an adenoma and leading to the carcinoma state. The tumor suppressor gene adenomatous polyposis coli (*APC*) is the first to suffer a mutation, leading to the formation of polyps, non-malignant adenomas, from which about 15% have a high chance of becoming carcinomas within a ten year time span[18]. Following the *APC* mutation CRC progression is accompanied by mutations in *KRAS*, *TP53* and *DCC* genes.

Inherited CRC cases account for 30% of all cases and are divided into two groups regarding the formation of polyps or lack thereof. The non-polyp variant is mainly comprised of hereditary non-polyposis colorectal cancer cases (HNPCC) also known as Lynch syndrome accounting for 5% of all CRC cases. HNPCC is caused by germline mutations in DNA mismatch repair genes *MLH1, MSH2, MSH6, PMS1* and PMS2 that are inherited in an autosomal dominant manner.[18,19,21]On the other hand the polyp formation variant is mostly comprised of familial adenomatous polyposis cases (FAP) and is caused by germ-like mutations in the *APC* gene causing the formation of more than 100 adenomatous polyps, each with a 15% chance to progress into an adenocarcinoma, with an autosomal dominant inheritance.[18–20]

HNPCC and FAP represent the most commonly occurring cases of non-polyp and polyp variants of inherited CRC however, there are also many other closely related variant syndromes that are part of inherited CRC.[18,22]

1.2 The role of Lysosomes in Cancer Cell Survival

Lysosomes are membrane bound vesicles containing an array of hydrolases and are the most acidic vesicles in the cells, playing a key role in the degradation, recycling, and disposal of several cellular macromolecules. Vesicle fusion with the lysosomes, allowing the release of hydrolases for the degradation of vesicular contents, is a crucial step for the maintenance of cellular homeostasis in cellular processes such as autophagy, endocytosis and phagocytosis.[23,24]Additionally, lysosomes also play a role in the regulation of cell signaling, metabolism[25] and cell death[26].

Cancer cells show an increase in lysosome biogenesis, with a higher expression of lysosomal proteins and enzymes that promote tumor progression and metastasis, and a decrease in the expression of lysosomal proteins necessary for lysosome associated cell death. An increase in the number of lysosomes results in increased macromolecule degradation and recycling generating nutrients to sustain cellular proliferation and also play a role in drug resistance. As such lysosomes represent promising targets for cancer therapies.[27,28]

1.2.1 Autophagy

As a highly conserved evolutionary cellular degradation process, autophagy is characterized as the degradation of long-lived or dysfunctional organelles and proteins. There are three types of autophagy, macroautophagy, where the formation of an autophagosome occurs followed by fusion with a lysosome forming an autolysosome, microautophagy, where the lysosome engulfs a small part of the cytoplasm through an inward invagination of its membrane, and chaperone mediated autophagy where substrate proteins harboring chaperones are recognized by the Lysosome associated membrane protein 2A (LAMP2A) that acts as a receptor and are directly translocated across the lysosomal membrane. Since macroautophagy is thought to be the main type of autophagy and has been studied to a greater extent, macroautophagy will be referred to as autophagy from here on.

The process of autophagy is accomplished through the formation of a phagophore that will surround dysfunctional organelles and ubiquitinated proteins, forming an autophagosome which will then fuse with a lysosome resulting in an autolysosome where the cellular contents are degraded by the released lysosomal enzymes (**Figure 1.4**). In normal cells, autophagy is usually triggered as a response to hypoxia, nutrient deprivation, and stress as an attempt to maintain homeostasis.[29,30] However, in cancer cells this defensive response can be used to promote cell proliferation and ensure cell survival against therapeutic drugs that induce cellular stress.[31]

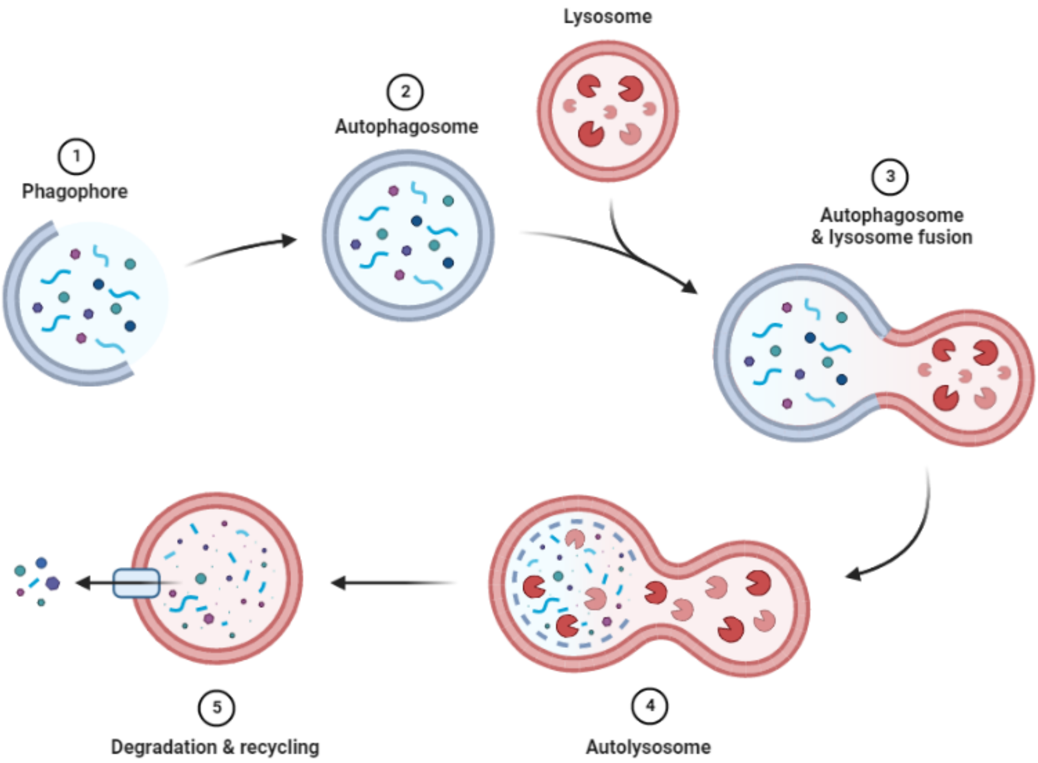

Figure 1.4- *Representation of the Autophagy process. A phagophore membrane starts elongating around dysfunctional organelles or ubiquitinated proteins forming an autophagosome, which will come in contact and fuse with hydrolase filled lysosomes forming and Autolysosome with the release of hydrolases resulting in the degradation of the molecules inside it. Created with Biorender.com.*

1.2.2 Autophagy in cancer

Autophagy has two contradictory roles when it comes to carcinogenesis (**Figure 1.5**). Autophagy acts as a tumor suppressor during the early stages of the transition from a normal cell to a cancer cell, removing damaged organelles, reactive oxygen species, damaged mitochondria, and aggregates of ubiquitinated protein, preventing the accumulation of genetic defects by clearing mutagens and ensuring genome stability, promoting autophagic cell death, limiting inflammation which inhibits malignant transformation that would be stimulated by the inflammation caused by the tumor microenviroment[32] and is also the first line of defense against viral and bacterial infections, that can be the underlying cause for the appearance of colorectal cancer.[33] Studies have shown that the inhibition of autophagy promotes the activation of oncogenes and leads to the development of cancer cells.[34,35]In later stages during the progression of tumors, cancer cells are under various stresses, being exposed to hypoxia, nutrient deprivation, selective pressure due to therapeutic intervention, and metabolic stress, due to their very high proliferation rate and as such the high needs of both ATP and metabolites.[36] In this case autophagy ends up promoting cancer progression, since it is a mechanism activated during starvation or stress, providing a backup energy source for cell survival and expansion, while enhancing drug resistance, and ensuring cell survival by inhibiting cell death or promoting survival in a dormant state and by reducing tumor sensitivity to harming stimuli.[33,37]

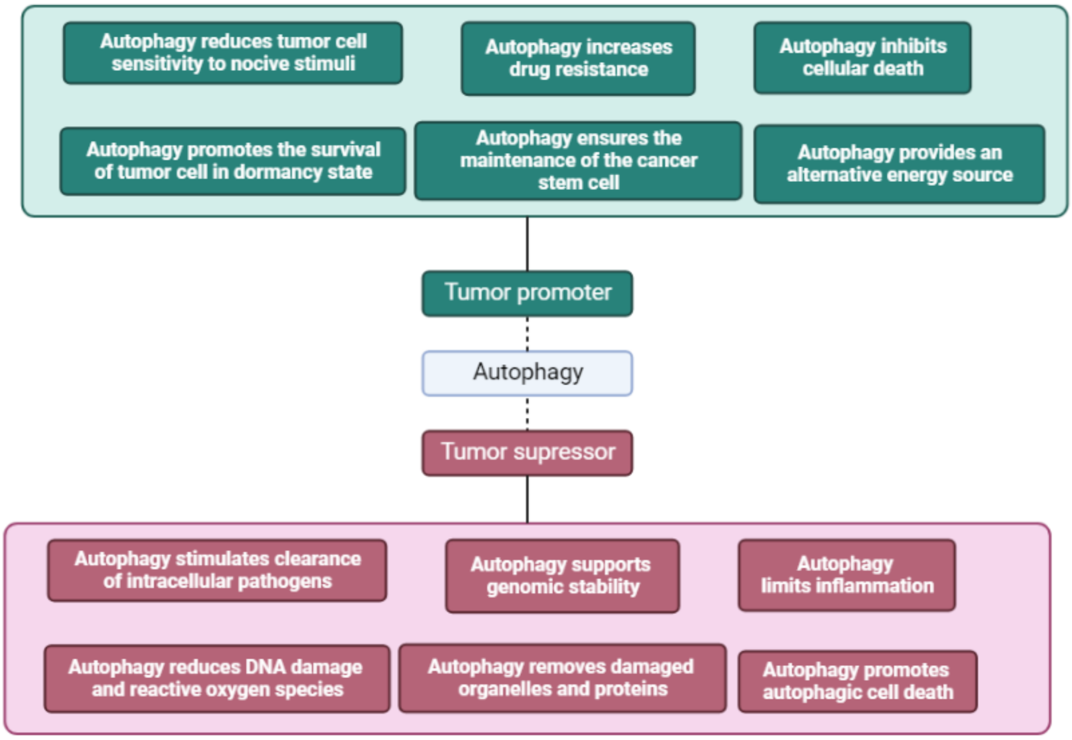

Figure 1.5- ***The dual and contradictory roles of autophagy in cancer.*** *Depending on the state of tumor development autophagy can act as an inhibitor of the transformation from normal to cancer cell or promote tumor development. Autophagy suppresses the transition of normal cell to cancer cell by removing damaged organelles and proteins, reducing DNA damage and reactive oxygen species, supporting genomic stability, promoting autophagic cell death, limiting inflammation and stimulating the clearance of intracellular pathogens. Autophagy promotes tumor development by providing an alternative energy source, increasing drug resistance, inhibiting cell death, promoting the survival of tumor cells in a dormant state, and ensuring the maintenance of cancer stem cell compartments. Adapted from* [33] *and created with Biorender.com.*

1.3 Cancer therapies

Due to the heterogeneity and complexity of cancer there is not a standardized treatment to follow, and several methodologies of treatment are implemented. The best methodology is chosen by considering the type of cancer as well as its level of progression. The most conventional therapies currently used are surgery, chemotherapy, and radiotherapy. However, these conventional therapies harbor multiple disadvantages, which restricts their effectiveness since there is incomplete tumor eradication giving room for recurrence with the appearance of resistant cancer cells, lack of selectivity which ends up killing normal cells including effective immune cells and side effects caused by local and systemic toxicity from the treatment. Nevertheless the combined use of these therapies along with new approaches, that have emerged due to recent advancements regarding the understanding of molecular mechanisms of tumor resistance, has proven to be rather effective.[38–40]

1.3.1 Nanotechnology and the Rise of Nanomedicine

Nanotechnology is characterized as the manipulation of matter at the nanometer scale, resulting in the design and application of systems at the nanoscale (10^{-9}m). At this scale nanomaterials exhibit unique physical and chemical properties when compared to their bulk properties, having a high surface area to volume ratio, optical, electronic, magnetic and biological properties that can easily be modified, presenting a synthesis with complete control of size, shape, structures, and surface chemistry[41]. Thus, giving rise to what is now known as nanomedicine. Studies regarding the applications of an array of nanomaterials such as nanoparticles[42], show potential solutions for the main problems that cancer therapies face such as the lack of selectivity, drug clearance, biodegradation and low specificity.[43–45]Nanomedicine has the potential to revolutionize medicine in the areas of drug delivery, diagnosis and imaging.[46,47]The use of nanoparticles as drug carriers offers enormous advantages allowing for a reduction in drug dosage whilst ensuring pharmaceutical effects and minimizing side effects since particles protect drugs against degradation and enhance drug stability, plus nanoparticles can easily allow drug accumulation by penetrating through small capillaries and being taken up by cells[48,49], in addition nanoparticles can also act as imaging tools for diagnosis[49,50]Through the combination of their therapeutic and diagnostic effects nanoparticles have the ability to act as theragnostic systems.[49,51]

1.3.2 Nanoparticles in drug delivery and targeting

As previously mentioned, currently implemented cancer therapies although somewhat effective harbor many side effects which hinder their effectiveness. The use of nanoparticles as drug delivery systems (DDS) have shown very promising results, since nanoparticle properties can be tuned in their synthesis allowing for an optimized approach when dealing with different therapeutical targets.[52]

In cancer therapies nanoparticle-based DDS are designed for both active and passive targeting (**Figure 1.6**) of cancer cells maximizing nanoparticle accumulation in tumors. Passive targeting consists in the transport of nanoparticles through leaky tumor capillary fenestrations or passive diffusion into the tumor *interstitium*, there selective nanoparticle accumulation and retention occurs through the enhanced permeability and retention (EPR) effect observed in some solid tumours[53]. In other cases, due to elevated viscous and geometrical resistance, consequence of the heterogeneous nature of tumor induced capillaries, blood flow is compromised and combined with interstitial hypertension caused by poor lymphatic drainage and fluid leakage from the tumor vessels the efficacy and delivery of therapeutic drugs by DDS is reduced.[54] Active targeting in drug delivery is achieved through molecular recognition of specific ligands, such as antibodies for example, attached to the surface of nanoparticles through surface functionalization, meaning that nanoparticle DDS active targeting can easily be altered for optimal drug delivery in several different cancer scenarios. [55–58]

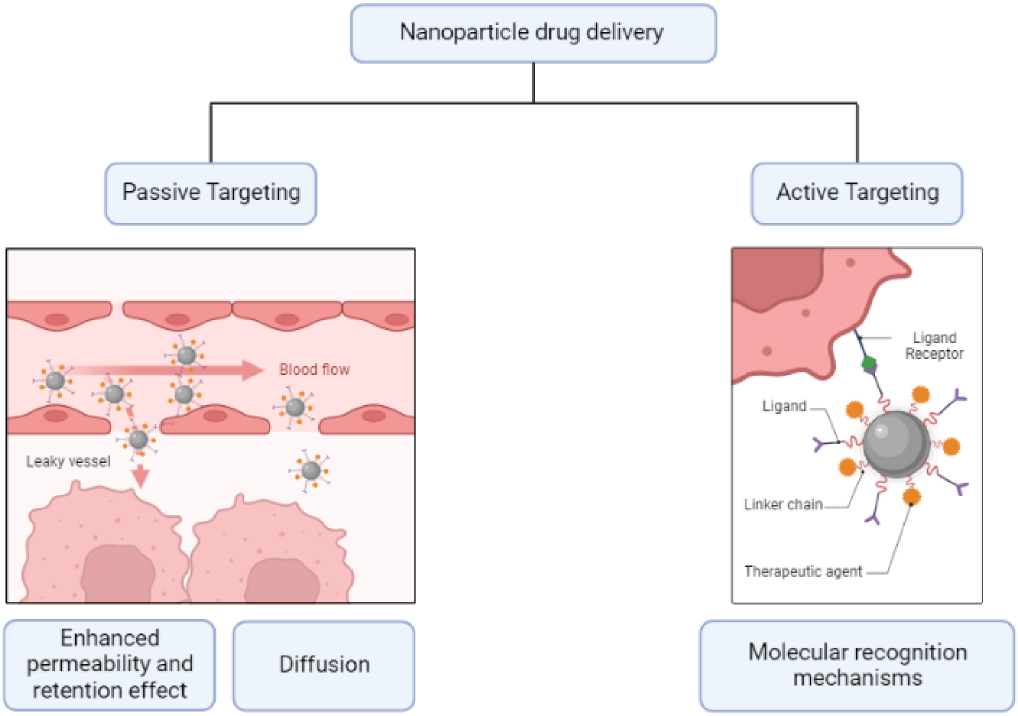

Figure 1.6- ***Nanoparticle drug delivery system targeting mechanisms.*** *Nanoparticle-based drug delivery systems can reach tumors via active or passive targeting. Passive targeting occurs when nanoparticles can reach the tumor microenvironment due to the irregular nature of tumor associated vessels causing an enhanced permeability and retention effect (EPR) and enhancing diffusion. Active targeting occurs through the molecular recognition of specific ligands, such as antibodies for example, attached to the surface of nanoparticles through surface functionalization. Created using Biorender.com.*

1.3.3 Cellular uptake of Nanoparticles

After reaching the target, nanoparticles enter the cell via the endocytic route, more specifically through phagocytosis or pinocytosis (**Figure 1.7**). Larger particles usually enter the cell via phagocytosis or macropinocytosis, whilst smaller particles, with sizes lower than 200nm enter the cell via micropinocytosis, more specifically through clathrin-dependent or caveolae-dependent routes. In the clathrin-dependent pathway the nanoparticles are wrapped inside a vesicle by the action of clathrin-1 forming a clathrin coated vesicle that can either be transported to the lysosomes or recycled back to the extracellular space. In the caveolae-dependent pathway nanoparticles are transported inside caveosomes, bypassing lysosomes, and are translocated to the endoplasmic reticulum or Golgi body.[56,59]

Nanoparticles for drug delivery usually have sizes ranging from 10 nm to 100nm, particle size needs to be lower than 100 nm so that extravasation from the fenestrations in leaky vasculature is efficient and particles can evade capture from the liver, and need to be bigger than 10 nm to avoid filtration by the kidneys.[58] As such nanoparticle DDS usually enter the cells via micropinocytosis. The route of entry in cells is dictated by nanoparticle properties.[60,61]

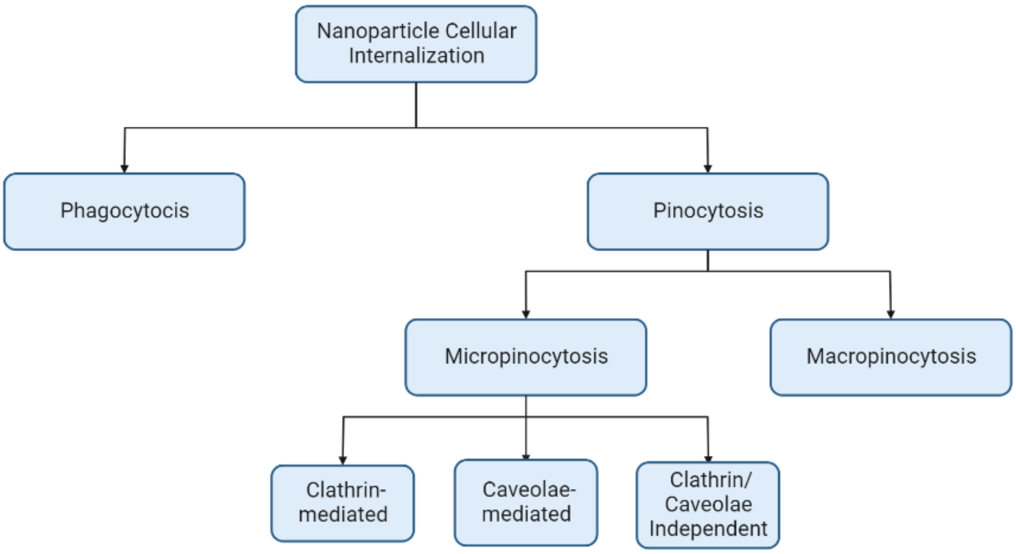

Figure 1.7- ***Nanoparticle cellular internalization pathways.*** *Nanoparticle-based drug delivery systems are designed with an optimized particle size, from 10 to 100nm, ensuring the internalization of particles via the different micropinocytosis routes, which can be manipulated through the functionalization of nanoparticles with specific molecules "controlling" the route by which nanoparticles enter the cell. Adapted from* [56] *and created with Biorender.com.*

1.3.4 Gold Nanoparticles

There are various kinds of nanoparticles that can be utilized in nanomedicine such as polymer-based nanoparticles, dendrimers, lipid-based nanoparticles, protein nanoparticles and inorganic nanoparticles which include ceramic, magnetic, carbon and gold nanoparticles.[62] However in recent years there has been an increase in studies regarding gold nanoparticle (AuNP) applications in imaging, diagnosis and targeted theraphy.[63–65]

The reason behind the interest in AuNPs resides in their unique chemical and physical properties such as an easy and simple synthesis process through the reduction of chloroauric acid with citrate (Turkevich method)[66], resulting in particles whose size, shape and surface properties can be tuned and optimized for the desired study, high absorption and light scattering efficiency, high photothermal conversion rate, high biocompatibility and low toxicity, with spherical AuNPs being the most stable and less toxic among metallic nanoparticles.[67,68]

AuNPs have a unique optical property called the localized surface plasmon resonance (LSPR) in which the electrons on the metal surface undergo a collective oscillation when excited by light at specific wavelengths causing AuNP absorption and scattering intensities to be much higher than other nanoparticles with the same size but lacking an LSPR effect. Generally, 14nm AuNPs have an LSPR peak at 520nm however, the LSPR peak can easily be tuned by changing particle size and shape to be able to absorb even in the near infrared (NIR) wavelengths which is of particular interest in biomedical applications because effective tissue penetration can be achieved in NIR.[69–71]

Furthermore, the surface of AuNPs can easily be functionalized with different molecules, through gold-thiol conjugation chemistry, to increase their already high biocompatibility, colloidal stability, solubility, circulation time and depending on the coating molecule to even allow binding with proteins such as antibodies or fluorophores for example for simultaneous targeting and imaging, highlighting even more the potential that is brought from the multifunctionality of AuNPs.[72,73]Due to this multifunctionality AuNPs have been employed in a wide variety of studies such as drug delivery, gene therapy, radiotherapy, imaging and photothermal therapy.[62,65,74,75]

1.4 Photothermal Therapy in cancer therapy

The use of heat to eliminate cancer cells is nothing new, using heat sources such as radiofrequency, microwaves, ultrasound waves and more recently laser light to induce hyperthermia, a moderate increase in temperature, in the range of 41-47ºC, at a specific target site for a couple of minutes. Through hyperthermia treatment tumors can suffer irreversible cell damage, through the denaturation of proteins and the destabilization of cellular membranes. The use of laser light for hyperthermia treatments allows for confined thermal damage of cancer cells; however, its lack of selectivity is a major drawback. Photothermal therapy (PTT) is an approach where photothermal agents are employed in cancer cells and irradiated with a laser to achieve a selective heating of the tumor environment. The choice of photothermal agent is based on the strength of their absorption cross-sections and light to heat conversion efficiency.[76,77]

Due to their unique optical properties AuNPs, with their extremely efficient light to heat conversion properties, make the perfect photothermal agents for PTT, combined with the possibility of surface modification with several different molecules enabling specific targeting of overexpressed proteins in cancer cells resulting in increased AuNP accumulation at tumor sites, increasing biocompatibility, circulation time and also allowing for real-time optical imaging of the target site (nanotheranostics), plus the ability to change AuNP LSPR peak to enable irradiation with different wavelengths without losing any light absorption and scattering efficiency. Through the combination of AuNP properties the implementation of combined therapies such as drug delivery followed by PTT is more than possible.[64,78–81]

1.5 Context and objectives

The implementation of nanoparticles, more specifically AuNPs, in cancer therapies could represent a future in which tumors can be quickly identified and dealt with through gene therapy, drug delivery, PTT and several other approaches.

Lysosomes are prime targets for cancer therapy. As discussed above autophagy can have a major role in promoting tumor proliferation but is extremely reliant in the existence of functional lysosomes. If the lysosomal integrity would be disrupted there would be no fusion with the autophagosome and consequently no degradation of any molecules inside it, meaning that there would be no recycling of metabolites, shutting down the much-needed alternative energy source for cancer cells to be able to proliferate and cell survival would be compromised, since there would be no protection from drugs or inhibition of cell death. Through the targeting of the lysosomes the tumor promoting mechanism of autophagy would be jeopardized making these molecules the perfect choice for targeted cancer therapies.

The lysosomal membrane consists of a lipid bilayer and membrane proteins. Lysosome associated membrane proteins 1 and 2 (LAMP1 and LAMP2) are the most abundant proteins in the lysosomal membrane. These proteins present a high degree glycosylation protecting the lysosomal membrane from digestion of its own hydrolases.[27,82,83] Studies have shown that a decrease in LAMP1 and LAMP2 proteins makes cancer cells more sensitive to Lysosome membrane permeabilization (LMP)[84], in which there is slight or complete permeabilization of the lysosomal membrane with the release of the lysosomal contents that can end up mediating cell death.[85–87]

As such the LAMP1 and LAMP2 proteins represent a possible target for an effective disruption of the lysosomes in cancer therapy.

The major objective of this thesis is to design and synthesize bioconjugated AuNPs capable of specifically targeting the lysosomes, and then apply photoirradiation to trigger optimized cell death – death from within. This should be attained via several intermediate objectives:

- Synthesis and characterization of AuNPs, which shall then be functionalized with specific antibodies towards recognition of LAMP2 in the lysosome.

- evaluate the internalization of the synthesized nanoconjugates by colorectal cell lines and study the effects of the accumulation of antibody functionalized AuNPs in the lysosome
- To test the effects of mild photothermy conditions in cell viability and organelle integrity.

2

MATERIALS AND METHODS

2.1 Synthesis of citrate capped gold nanoparticles

The synthesis of gold nanoparticles (AuNPs) was performed according to the protocol in Fernandes et al[88] which relies on the citrate reduction method described by Lee and Meisel[89], and that has been optimized to yield citrate capped gold nanoparticles (AuNP) with about 14nm. Gold salts are reduced to zero valence atoms, resulting in the formation of AuNPs and the citrate capping confers a negative charge to the nanoparticles attracting positively charged cations present in the solution, resulting in the formation of a diffuse electrical double layer that prevents AuNP aggregation and thus ensuring colloidal stability[90,91].

Before the synthesis, one must ensure that all glass material has been cleaned and is devoid of any traces of metal ions. As such, aqua regia was prepared in a hood by mixing three parts hydrochloric acid (HCL) with one-part nitric acid (HNO3) and allowed to react for a couple hours. Nanoparticle synthesis material was thoroughly washed with aqua regia to ensure that no metal or organic contaminants were present. Synthesis material was then washed with copious amounts of water until deionized water pH was attained to ensure no aqua regia was present.

Then, an aqueous solution of tetrachloroauric acid (HAuCl4) (225mL, 1mM) was brought to boiling until reflux begins. Then, a heated aqueous trisodium citrate solution (25mL, 38.8mM) was added and the solution continuously stirred for 30mins. The observation of a change in color from yellow to a dark red immediately after the addition of citrate, indicates the formation of the nanoparticles. The solution was allowed to cool at room temperature (RT). Lastly, using a 0.22µm syringe filter (Vented Milex ®-GV, Merck Millipore), the synthesized AuNP were sterilized and stored at RT away from light.

2.2 Citrate capped AuNP functionalization with PEG-COOH

2.2.1 AuNP Pegylation

Polyethylene glycol (PEG), a coiled polymer of repeating ethylene ether units with dynamic and flexible conformations, is a hydrophilic molecule characterized by its high biocompatibility and low toxicity. PEG is commonly used to functionalize AuNPs improving their in vivo stability, biocompatibility and provide conjugation sites for therapeutic agents and targeting ligands.[92,93]

Functionalization of citrate capped AuNPs was performed with molecules of PEG harboring a carboxylic acid functional group on one end (SH-EG(8)-COOH) (PEG-COOH) (458,57 g/mol) (Iris Biotech) (**Figure 2.1**), to allow for further functionalization with molecules harboring an available amine group through peptide bonding.

In this work to achieve 100% PEG-COOH coverage[94], a solution of 10nM of citrate capped AuNPs, PEG-COOH (0.01mg/mL) and 0.028% sodium dodecyl sulfate (SDS) was incubated for 16h. Excess PEG-COOH chains were removed by centrifugation at 14000xg for 30 min at 4ºC (Refrigerated SIGMA 3-16K centrifuge, Sartorius, Germany) and PEG-COOH coverage determined in section **2.2.2**. AuNP@PEG-COOH were resuspended in MiliQ H2O and stored at 4ºC.

Figure 2.1- *Representation of citrate capped gold nanoparticle (AuNP) functionalization with polyethylene glycol harboring a carboxylic acid functional group (SH-EG(8)-COOH) (PEG-COOH).*

2.2.2 Ellman´s Assay

Ellman’s assay, exploits the reaction of 5,5’-dithiobis-(2-nitrobenzoic acid) (DTNB or Ellman’s reagent) with thiolate anions leading to the formation of 2-nitro-5-thiobenzoic acid, an optically active compound that can be photometrically detected at 412nm, and is usually used to directly quantify thiol groups in solution.[95] Using this assay excess PEG-COOH chains, obtained in section **2.2.1**, were quantified to determine the degree of PEG-COOH coverage on the AuNPs.

Briefly standard solutions of PEG-COOH ranging from 0.0002-0.035mg/mL in 0.5M pH 7 phosphate buffer were prepared. The standard solutions and PEG-COOH chains were incubated for 10mins with 7µl of DTNB at RT and the absorbances at 412 nm measured with a Tecan Infinite M200 microplate reader (Tecan, Männedorf, Switzerland). Excess PEG-COOH concentration was determined through a calibration curve (See **Figure A1** in **annex A**) with the measurements of the standard solutions, and reaction efficiency calculated through **Equation 2.1**.

Equation 2.1:

$$\text{Efficiency (\%)} = \frac{\mathit{Inicial}\ [\text{PEG}-\text{COOH}](\text{mg/mL}) - \text{Supernatant}\ [\text{PEG}-\text{COOH}](\text{mg/mL})}{\mathit{Inicial}\ [\text{PEG}-\text{COOH}](\text{mg/mL})} \text{X}100$$

2.3 AuNP@PEG-COOH functionalization with Anti-LAMP2A

Colorectal cancer cells are highly dependent on autophagy as a backup energy generation mechanism, having an increase in lysosomal biogenesis with overexpression of lysosomal membrane proteins such as lysosomal associated membrane protein 2A (LAMP2A), that works as a receptor in the lysosomal membrane.[96]

AuNP@PEG-COOH functionalization with Abcam recombinant Anti-LAMP2A antibody [EPR4207(2)]- Lysosome Marker (ab125068) allows for an active targeting of the lysosomal membrane through molecular recognition of LAMP2A in colorectal cancer cells.

Optimal Functionalization is achieved via EDC/NHS coupling reaction at pH6 (**Figure 2.2**). EDC reacts with the carboxylic acid groups in PEG-COOH forming an active O-acylisourea intermediate, that is unstable in an aqueous solution and will hydrolyze regenerating the carboxyl group if an amine is not found. Reaction efficiency is improved through the addition of NHS, in the presence of sulfo-NHS (NHS water soluble analogue), EDC couples NHS to the carboxyl group forming an amine-reactive NHS ester that is significantly more stable than the O-acylisourea intermediate allowing for a more efficient conjugation to the primary amines present in the Anti-LAMP2A antibody.[97]

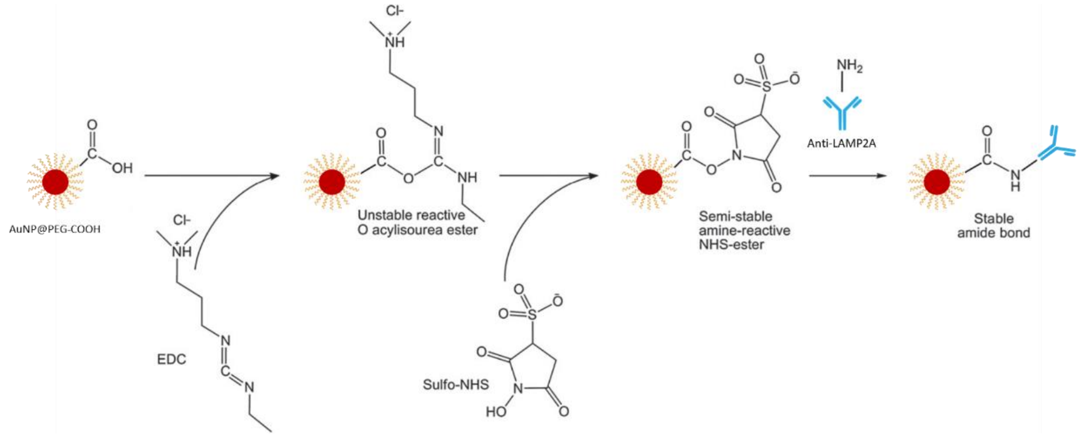

Figure 2.2- ***Representation of AuNP@PEG-COOH functionalization with Anti-LAMP2A antibody [EPR4207(2)]- Lysosome Marker (ab125068) through EDC/NHS coupling reaction.*** *EDC reacts with the carboxylic acid groups in PEG-COOH forming an active O-acylisourea intermediate, in the presence of sulfo-NHS (NHS water soluble analog) EDC will couple NHS to the carboxyl group forming an amine-reactive NHS ester that is significantly more stable than the O-acylisourea intermediate allowing for a more efficient conjugation to the primary amines present in the Anti-LAMP2A antibody. Adapted from*[97]

2.3.1 Functionalization with the Antibody

To achieve maximum antibody coverage of AuNP@PEG-COOH superficial area (see **Figure A2** in **annex A**), a 10mM pH6 MES buffer solution containing 21nM AuNP@PEG-COOH, 1.25mg/mL Sulfo-NHS and 0.312mg/mL EDC was incubated for 30mins at RT, centrifuged at 14000xg for 30 min at 4ºC (Refrigerated SIGMA 3-16K centrifuge, Sartorius, Germany), the supernatant removed and pellet resuspended in 2.5mM pH6 MES buffer. Salt concentration is reduced to ensure particle stability. Anti-LAMP2A antibody was added, at an optimal concentration for maximum coverage, to the AuNP@PEG-COOH, now with semi-stable amine reactive NHS esters ready to form a peptide bond with free amine groups, and the solution incubated for 16h. Excess antibody removed through centrifugation at 14000xg for 20 min at 4ºC and reaction yield determined in section **2.3.2**. The AuNP@PEG-COOH@Anti-LAMP2A were resuspended in MiliQ H2O and stored at 4ºC to avoid antibody denaturation.

2.3.2 Bradford Assay

The Bradford protein assay is generally used to determine protein concentrations in samples, through the binding of the Coomassie dye to protein molecules which causes an immediate shift in the absorption maximum of the dye from 465nm to 595nm accompanied by a change in solution color from brown to blue. Through this assay excess antibody concentration, obtained in section **2.3.1**, was quantified and the yield of AuNP@PEG-COOH antibody functionalization reaction determined.

Using the Pierce™ Coomassie (Bradford) Protein Assay Kit (23200) (Thermo scientific™, USA), standard solutions of bovine serum albumin (BSA) in 2.5mM pH 6 MES buffer with concentrations ranging from 0-25μg/mL were prepared. Then 75 μL of standard solutions and excess antibody were incubated for 10mins with 75μL of Coomassie reagent at RT and the absorbances at 595 nm measured with a Tecan Infinite M200 microplate reader (Tecan, Männedorf, Switzerland). Excess antibody concentration was determined through a calibration curve (See **Figure A3** in **annex A**) with the measurements of the standard solutions, and reaction yield calculated through **Equation 2.2**.

Equation 2.2:

$$\text{Efficiency (\%)} = \frac{\mathit{Inicial}\ [\text{Anti}-\text{LAMP2A}](\mu\text{g/mL}) - \text{Supernatant}\ [\text{Anti}-\text{LAMP2A}](\mu\text{g/mL})}{\mathit{Inicial}\ [\text{Anti}-\text{LAMP2A}](\mu\text{g/mL})} \text{X}100$$

2.4 Gold nanoparticle characterization

For UV-Visible Spectrophotometry, Dynamic light scattering (DLS) and zeta potential characterizations samples were analyzed in triplicates for AuNPs and AuNP@PEG-COOH. AuNP@PEG-COOH@Anti-LAMP2A samples were analyzed individually and only characterized through UV-Visible Spectrophotometry due to low particle concentration, consequence of low particle stability that resulted in precipitation.

2.4.1 AuNP characterization by UV-Visible Spectrophotometry

AuNP UV-visible spectrophotometry characterization was performed through a method developed by Heiss et. al[98] allowing the estimation of citrated capped AuNPs diameter and molar extinction coefficient to determine particle concentrations. Citrate capped AuNP diameter was determined using the calibration curved performed by Heiss et al (see **Figure A4** in

annex A) and the absorbance values at the Localized surface plasmon resonance (LSPR) peak and at 450nm.

AuNPs spectrums were obtained (UVmini-1240 Shimadzu, Kyoto, Japan), in the wavelength range of 750-400nm using a 1cm optical path quartz cuvette at RT and nanoparticle concentrations determined through the Lamber-Beer law using the corresponding absorbance value of the LSPR peak with a molar extinction coefficient of 2.33×10^8 M^{-1} cm^{-1}.

2.4.2 DLS and Zeta Potential

DLS is a technique used to measure particle size through the fluctuation in the intensity of light that is scattered when passing through the particles. This fluctuation in intensity occurs due to the Brownian motion of particles, described as the random movement of particles in a solution consequence of their collision with solvent molecules, in which smaller particles tend to move more quickly and larger particles more slowly. DLS measures the size of a sphere that is comprised of the core particle and any ions or absorbed polymers in the surface of the particle, meaning that it measures the hydrodynamic size of the particle.[99,100]

Zeta potential, also referred to as electrokinetic potential, reflects the potential difference between charged particles and dispersant molecules when under the influence of an applied electric field. Zeta potential analysis is performed to evaluate particle stability in a colloidal solution.[100,101]

Prior to analysis the AuNP samples were diluted in MiliQ H_2O to a final concentration of 4nM. The zeta potential analysis of AuNPs solutions was performed simultaneously with the DLS analysis, using Nanoparticle Analyser SZ-100 (Malvern Panalytical), as a service (Nano4 Global, Lda).

2.5 Cell Culture

HCT116 colorectal carcinoma cells (ATCC® CCL-247™) were grown in Dulbecco's Modified Eagle Medium (DMEM) (Gibco^{TM} by Life Technologies, Invitrogen, California, USA) (with phenol red indicator) supplemented with 10% (v/v) Fetal Bovine Serum (FBS) 1% (v/v) Penicillin/Streptomycin solution and maintained in $25cm^3$ T-Flasks at 37ºC in a 99 % humidified atmosphere of 5 % (v/v) CO_2 (SANYO CO2 Incubator, Electric Biomedical Co., Osaka, Japan).

2.5.1 Cell culture maintenance

Cells were sub-cultured to maintain exponential growth and to avoid loss of growth due to lack of nutrients and contact inhibition. As such every week, when cells achieved a state of about 80-90% confluence, culture medium was removed and discarded, 2 mL of PBS 1X added, to remove leftover medium ensuring that trypsin activity would not be inhibited, and discarded, 2mL of TrypLE^{TM} Express (Gibco®, New York, EUA) were added and incubated for 5min in the CO_2 incubator to promote cell detachment, then 2mL of DMEM were added to block trypsin activity. The cell suspension was transferred to two 2 ml Eppendorf's and centrifuged (Sigma 1-14 microcentrifuge, Germany) at 500xg for 5min at RT, the supernatant removed, and the cells resuspended and concentrated in 1mL of fresh DMEM medium.

Living cells were counted by the Trypan blue exclusion method in a hemocytometer (Hirschmann, Eberstadt, Germany). This method is based on the principle that living cells possess intact membranes that exclude certain dyes such as trypan blue whereas dead cells do not. To that end 350µL of DMEM, 50µL of the obtained cell suspension and 100µL of a 0.4% (v/v) Trypan blue solution (Sigma, St. Louis, EUA) were mixed. Living cells were directly observed and counted through an optical inverted microscope (Nikon TMS, Nikon Instruments, Tokyo, Japan), and cell density determined through **Equation 2.3**

Equation 2.3:

$$\text{Cell density (cells/mL)} = \frac{\text{Number of viable cells x } 10^4 \text{ x } 10 \text{ (dilution factor)}}{\text{Number of squares}}$$

Cells were seeded at 7.5x10^4 Cells/mL in a 25cm^3 T-Flask supplemented with 5mL of DMEM medium and maintained in a 99 % humidified atmosphere of 5 % (v/v) CO_2 (SANYO CO2 Incubator, Electric Biomedical Co., Osaka, Japan).

Cell cultures were weekly analyzed for the presence of mycoplasma contaminants by polymerase chain reaction performed by lab members.

2.6 Cell Challenge with Gold Nanoparticles

Challenge of the HCT116 cells with the AuNP@PEG-COOH and AuNP@PEG-COOH@Anti-LAMP2A was performed to enable studies regarding the uptake of nanoparticles by the cells and evaluate the targeting of the lysosomes and their effect on cell viability through photothermy assays.

For that HCT116 cells were seeded at a density of $2x10^4$cells per well in a 96well plate (SPL Life Sciences, South Korea) for 24h at 37ºC in a 99 % humidified atmosphere of 5 % (v/v) CO_2, the medium replaced with fresh medium containing 2.5nM of AuNP@PEG-COOH or 2.5nM of AuNP@PEG-COOH@Anti-LAMP2A in study wells and fresh medium in control wells, followed by another 24h incubation in the same conditions.

Cellular uptake was then determined through U.V-visible spectrophotometry and inductively coupled plasma atomic emission spectroscopy (ICP-AES).

2.6.1 Assessment of AuNP uptake through U.V-visible spectrophotometry

AuNP uptake was quantified through U.V-visible spectrophotometry to study the influence of Anti-LAMP2A functionalization in cellular uptake of the AuNP@PEG-COOH@Anti-LAMP2A.

After the 24 h incubation period U.V-vis spectrums of all wells were taken using a Tecan Infinite M200 microplate reader (Tecan, Männedorf, Switzerland) and total particle concentration determined as described in section **2.4.1**. The medium of all wells transferred to another 96 well plate (SPL Life Sciences, South Korea) and particle concentration in the medium determined. Cellular particle concentration was determined by subtracting particle concentration in the medium to the total particle concentration. **(Equation 2.4)**

Equation 2.4:

$$\text{Cellular [AuNP]} = \text{Total [AuNP]} - \text{Medium [AuNP]})$$

2.6.2 Fractionating of Challenged Cells

Cell challenge was performed as described in section **2.6** with the exception that cells were seeded at a density of $1x10^5$ cells per well in a 24 well plate (SPL Life Sciences, South Korea).Then medium from each well was removed and stored in Eppendorf's, the wells washed twice with 500µL of PBS 1X that was also then stored in the same Eppendorf's, cells detached and centrifuged as described in section **2.5.1**, with the exception that 250 µL of TrypLE^{TM} Express (Gibco®, New York, EUA) and DMEM medium were used instead of 2 mL, supernatants removed and stored in the Eppendorf's containing the mediums and PBS 1X at 4 ºC. Using the

Abcam Cell Fractionation Kit - Standard (ab109719) cells were resuspended, fractionated and cytosolic, mitochondrial, and nuclear fractions obtained through differential precipitation of fraction density.

2.6.3 ICP-AES

ICP-AES is an analytical technique capable of detecting even trace amounts of chemical elements in samples. ICP-AES was performed to quantify nanoparticle accumulation in different cell fractions and study the influence of Anti-LAMP2A functionalization (AuNP@PEG-COOH@Anti-LAMP2A) in active targeting of the lysosomes.

Fractionated samples preparation for ICP-AES analysis

After cell fractionation, aqua regia was prepared as described in section **2.1**, the stored supernatants transferred to 15 mL falcon tubes (SPL Life Sciences, South Korea), 2 mL of aqua regia were added to each falcon and left to react overnight. The same was done with the obtained cell fractions by adding 1 mL of aqua regia to each Eppendorf and left to react overnight. The addition of aqua regia is necessary for the dissolution of any gold (Au) present in the samples so that it can be quantified by ICP-AES. Afterwards samples were sent for ICP-AES analysis.

2.7 Assessment of Cell Viability

2.7.1 MTS Assay

Cell viability was assessed through MTS assay through CellTiter 96® AQueous One Solution Cell Proliferation Assay using 3-(4,5-Dimethylthiazol-2-yl)-5-(3-carboxymethoxyphenyl)-2-(4-sulfophenyl)-2H-tetrazolium (MTS). This colorimetric assay is based on MTS reduction in metabolically active cells by mitochondrial dehydrogenases due to the presence of phenazine methosulfate an electron coupling agent, generating a formazan dye that is soluble in culture media and can be quantified, by measuring the absorbance at 490nm, which is directly proportional to the number of metabolically active (viable) cells in culture .[102]

Cell challenge was performed as described in section **2.6**. Afterwards medium was removed and discarded, replaced with fresh medium containing an MTS solution (20µl of MTS in 80µl of DMEM per well), the plates incubated for 30 min in the same conditions. Then absorbance at 490nm was measured with a Tecan Infinite M200 microplate reader (Tecan, Männedorf, Switzerland) and cell viability calculated through **Equation 2.5**

Equation 2.5:

$$\text{Cell Viability (\%)} = \frac{Abs\ of\ the\ analysed\ sample - Abs(respective\ sample\ control)}{Abs\ of\ cell\ control - Abs\ of\ blank}\ \text{X}100$$

2.7.2 Trypan Blue Exclusion Method

Membrane integrity was determined via the Trypan blue exclusion method. Cell challenge was performed as described in section **2.6**. Cell density was determined as mentioned in section **2.5.1** and the percentage of living cells calculated through **Equation 2.6**

Equation 2.6:

$$\text{Living cells (\%)} = \frac{Cell\ density\ in\ study\ well}{Cell\ density\ in\ control\ well}\text{x}100$$

2.8 Western Blot

Western blot was performed to study the presence of lysosomes and AuNP@PEG-COOH@Anti-LAMP2A in the different cellular fractions.

2.8.1 Pierce Assay

The Pierce protein assay, generally used to determine protein concentrations in samples, is characterized by a change in color of a dye-metal complex from a reddish-brown to green upon protein binding. This color change is produced due to the facilitated interactions that happen at low pH between positively charged amino acid groups in proteins and the dye causing its deprotonation. This color change causes a shift in the dyes absorption maximum that can be measured at 660nm.

Cell challenge was performed, and cells fractionated as described in section **2.6.2** with the exception that cells were only incubated with AuNP@PEG-COOH@Anti-LAMP2A.

Using the Pierce™ 660nm Protein Assay Kit (22662) (Thermo Scientific™, MA, USA), BSA protein standard solutions, with concentrations ranging from 0-1000µg/mL, and protein samples from the cellular fractions, diluted 1:10 in MiliQ H_2O, were incubated with 150µL of Pierce reagent for 5min at RT, and absorbances at 660nm measured with a Tecan Infinite M200 microplate reader (Tecan, Männedorf, Switzerland). Protein concentrations were determined through a calibration curve (See **Figure A5** in **annex A**) with the measurements of the standard solutions. After quantification cell fractions were stored at -80 ºC to avoid protein denaturation.

2.8.2 Sample Preparation

Following western blot sample preparation step from the Abcam Cell Fractionation Kit - Standard (ab109719), 4.6µg of the cell fractions were incubated with a 5X SDS-PAGE sample buffer for 10 min in a 60 ºC water bath and vortexed. Due to low protein concentration in some fractions 4.6µg was the highest amount of protein that could be used for western blot analysis to ensure that all samples had equal amounts of protein without exceeding the maximum capacity of the wells.

2.8.3 SDS-PAGE Gel Electrophoresis and nitrocellulose membrane transfer

Incubated samples were immediately loaded into a 5% stacking, 10% resolving acrylamide/Bisacrylamide gel (SDS-PAGE) (see **Table 2.1** for SDS-PAGE gel composition), NZYtech's NZYColour Protein Marker II (MB090) was added to both ends of the gel and electrophoresis ran at 120 V for 90 min. Due to the denaturing conditions of the SDS-PAGE gel, the influence of protein structure and charge is eliminated, proteins acquire a negative charge, unfold into their linear chains and migrate through the gel according to the length of their polypeptide chain resulting in the separation of proteins by molecular weight.

After electrophoresis samples were transferred from the gel to a nitrocellulose membrane (Amersham^{TM} Protran^{TM} Premium 0.45µm NC, Sigma-Aldrich, USA) through a three-buffer semi-dry transfer system, (see **Table 2.2** for buffer compositions) at 130 mA for 1 h (see **Figure A6** in **Annex A**). Under these conditions the negatively charged proteins migrate towards the positive pole of the system and are transferred to the membrane.

Transfer efficiency was analyzed by staining the membrane with Ponceau solution and the SDS-PAGE gel with Coomassie blue. The membrane was incubated with ponceau solution for 5min at RT then washed twice with MiliQ H_20 to observe the transferred protein bands. The SDS-PAGE gel was incubated with Coomassie blue for 30 mins at 50ºC and washed twice with MiliQ H_20 to observe if any protein band was not transferred and still on the gel.

Table 2.1: *SDS-PAGE gel composition (5% stacking, 10% resolving acrylamide/bisacrylamide)*

	Resolving (10%)	**Stacking (5%)**
H_20	5mL	3.4mL
Acrylamide/bisacryldamide	2.5mL	830mL
Respective Buffer 4x*	2.5mL	630mL
20% SDS	25μL	25μL
10% APS	100μL	50μL
TEMED	10μL	5μL

*- Either Resolving Buffer 4x or Stacking Buffer according to the gel that is being prepared.

Table 2.2: *Semi-dry transfer system buffer composition*

Buffer	Composition
Cathode Buffer I	25 mM Tris, pH 9.4, 40 mM 6-aminohexanoic acid
Anode Buffer I	0.3 M Tris, pH 10.4
Anode Buffer II	25 mM Tris, pH 10.4

2.8.4 Membrane Blocking and Antibody Staining

Following protein transfer, membrane staining with specific primary and secondary antibodies was performed to determine the presence of lysosomes and AuNP@PEG-COOH@Anti-LAMP2A in the different cellular fractions.

The nitrocellulose membrane was blocked with a 5% (w/v) BSA (Nzytech, Lisbon) 1xTBST (50 mM Tris, 150 mM NaCl and 0.1% (v/v) Tween 20, pH 7.5) solution under agitation for 2 h at RT. Membrane blocking is essential to avoid non-specific antibody binding due to the high protein affinity of the membrane. The membrane was incubated with Anti-LAMP2A antibody [EPR4207(2)]- Lysosome Marker (ab125068) in 5% BSA (w/v) (Nzytech, Lisbon) 1xTBST (1:2000) overnight at 4 ºC, then to remove excess antibodies washed thrice with 1x TBST for 5mins under agitation. Afterwards the membrane was incubated with Cell Signaling anti-rabbit IgG, HRP-linked Antibody #7074 in 5% non-fat milk (w/v) 1xTBST(1:1000) for 1 h at RT, then washed thrice with 1x TBST for 5mins under agitation.

2.8.5 Film exposure

After antibody staining the membrane was incubated with a Western Bright ECL solution (Advansta, Menlo Park, California, USA) for 5 mins at RT. ECL is a horseradish peroxidase substrate optimized for chemiluminescent western blot imaging. After incubation, in a dark room, a film was exposed to the membrane and revealed. The film was then analyzed for the presence of LAMP2A regarding the different cellular fractions to determine the presence of lysosomes and AuNP@PEG-COOH@Anti-LAMP2A.

2.8.6 Membrane Stripping

Membrane stripping is done to remove antibody staining from the nitrocellulose membrane and allow for further staining of the same membrane with other antibodies.

For membrane stripping, the membrane was washed with 1xTBST, then incubated with stripping buffer (0.1 M glycine, 20 mM magnesium acetate, 50 mM potassium chloride, pH 2) for 10 mins at RT under agitation, stripping buffer was discarded, more Stripping buffer added, and the membrane incubated for another 20 mins under the same conditions, then washed with TBST.

2.8.7 β -Actin control

Western blot control was performed with β-actin, a protein that is generally expressed in all eukaryotic cell types and usually remains unaffected regardless of the experimental procedure, as a loading control to normalize the detected levels of protein ensuring that protein loading is the same across the gel.

Membrane blocking, primary and secondary antibody staining was performed as described in section **2.8.4**, using Cell Signaling anti-β-actin #3700 (1:5000) as primary antibody, and Cell Signaling anti-mouse IgG HPR-linked antibody #7076 (1:3000) as secondary antibody.

2.9 Immunofluorescence Microscopy

Immunofluorescence microscopy was performed to observe the cellular localization of AuNP@PEG-COOH@Anti-LAMP2A in HCT116 cells after a 24h incubation and verify if the particles were accumulated in the lysosomes proving the existence of an active targeting mechanism. For a clear observation, nuclei, lysosomes, and nanoparticles were stained with fluorescent molecules.

Nuclei were stained with Hoechst 33258 dye (Phenol, 4-[5-(4-methyl-1-piperazinyl)[2,5'-bi-1H-benzimidazol]-2'-yl]-, trihydrochloride 23491-45-4) (Molecular Probes® by Life Technologies, Invitrogen, California, USA), a nuclear dye that binds to DNA emitting blue fluorescence (excitation at 352nm and emission at 461nm), lysosomes stained with CellLight® Lysosomes-GFP *BacMam 2.0 (C10596), a viral vector system containing a mammalian promotor with the sequence for green fluorescent protein (GFP) for expression of lysosome-GFP fusion peptides which emit green fluorescence (excitation at 485nm and emission at 520nm) and AuNP@PEG-COOH@Anti-LAMP2A stained with Goat anti-rabbit IgG (TRITC (Tetramethylrhodamine isothiocyanante)) (ab6718) which emits red fluorescence (excitation at 547nm and emission at 572nm).

For a thorough analysis of AuNP@PEG-COOH@Anti-LAMP2A active targeting of the lysosomes, control groups of HCT116 cells and HCT116 cells incubated with AuNP@PEG-COOH stained with, Anti-LAMP2A antibody and Goat anti-rabbit IgG (TRITC) were also performed.

Lysosome staining

Following CellLight® Reagents *BacMam 2.0* protocol a solution of CellLight® Lysosomes-GFP *BacMam 2.0 was prepared in DMEM medium to achieve 100 particles per cell. HCT116 cells were seeded at a cellular density of $0.2x10^4$ cells per well in a 96 well plate (SPL Life Sciences, South Korea) for 24 h at 37ºC in a 99 % humidified atmosphere of 5 % (v/v) CO_2, medium was then replaced with the prepared CellLight reagent solution in the study wells, fresh medium in control wells and incubated for 48h in the same conditions, to allow enough time for the expression of the lysosome-GFP fusion peptides.

Hoechst and Antibody Staining

Cells were fixated with 100 µl of 4%(v/v) paraformaldehyde for 20 mins at RT, washed once with PBS 1X, cells were incubated with 100µl of Triton-X 100 (0.1%) in PBS 1X for 10 mins for membrane permeabilization to allow antibody staining of the lysosomes and washed again once with PBS 1X. Cell blocking was done with a 100µl of 1% BSA (w/v) PBS 1X solution for 30 mins at RT, to minimize unspecific binding of the primary antibody within the cell. Cells were incubated with 100µl of Anti-LAMP2A in 1% BSA (w/v) PBS 1X (1:200) for 1 h at RT, washed once with PBS 1X, then incubated with 100µl of Goat anti-rabbit IgG (TRITC) in 1% BSA (w/v) PBS 1X (1:1000) for 1 h at RT and washed again once with PBS 1X.

Then cells were incubated with 100 µl of Hoechst 33258 (7.5µg/mL) for 15 mins at RT, for nuclei staining, and washed once with PBS 1X.

Microscope Observation

Cells were visualized using a Ti-U Eclipse inverted microscope (Nikon, Tokyo, Japan). HCT116 cell images were obtained through brightfield, Hoechst-stained nuclei images were obtained with a DAPI filter (excitation at 360/40nm and emission at 460/50nm), lysosomes-GFP images obtained with a FITC filter (excitation at 480/30 nm and emission 535/40nm) and antibody Goat anti-rabbit IgG (TRITC) images were obtained with a G2A filter (excitation at 535/50nm in the blue region and emission at >590nm). All obtained fluorescence images were treated using the Image J software.

2.10 Photothermy Assay

A photothermal assay was performed to analyze AuNP@PEG-COOH@Anti-LAMP2A internalization/membrane adsorption and simultaneously evaluate, their abilities as photothermal agents, through their highly efficient light to heat conversion properties, to promote cell death or to disrupt cell growth in HCT116 cells by irradiating cells with a laser.

Cell challenge was performed as described in section **2.6,** with the exception that phenol red free DMEM medium was used instead of DMEM medium supplemented with phenol red. For a representation of the study and control well for photothermy assays see **Figure B1** in **Annex B**. Study wells were irradiated for 1 min with 2.37W/cm^2 using a continuous 532 nm green diode-pumped solid-state laser (Changchun New Industries Optoelectronics Tech. Co., LTD, Changchun, China) coupled to an optical fiber. The temperature of each well was registered before and after laser irradiation to quantify the heat generated through AuNP laser excitation. Cell viability was determined through MTS assay as described in section **2.7.1** and membrane integrity through Trypan Blue exclusion method as described in section **2.7.2**.

3

RESULTS AND DISCUSSION

The main objective of this thesis was to trigger optimized cell death through photoirradiation of the lysosomes. For that, a photothermal agent with a good light to heat conversion efficiency was necessary, but that agent would also need to be delivered or reach the lysosomes. In other words, there would need to be an active targeting to the lysosomes. Additionally, for eventual clinical, use this agent would need to be stable, biocompatible, and preferably have a low toxicity index. As such, gold nanoparticles (AuNPs) were chosen since they make for the perfect photothermal agent, due to their extremely efficient light to heat conversion[76–78] and their surface chemistry allows for easy functionalization with several different molecules allowing for an increase in particle stability, biocompatibility and active targeting of organelles[67,68,72].

3.1 Characterization of synthesized AuNPs

3.1.1 Characterization of Citrate Capped AuNPs

In this study, citrate capped gold nanoparticles (AuNP) were synthesized, as described in section **2.1** through the citrate reduction method in optimized conditions to obtain 14nm AuNPs. AuNPs were characterized through U.V-visible spectrophotometry as described in section **2.4.1** to observe the localized surface plasmon resonance (LSPR) peak and determine particle size and concentration. A spectrum of the AuNPs was obtained **(Figure 3.1),** where the LSPR peak was observed at 519nm (**Table 3.1**), then particle concentration determined through the lambert-Beer law at 10nM and the diameter through **Equation 3.1** at 14nm.

Equation 3.1:

$$\text{Diameter (nm)} = 0.112e^{2.9986\times(\text{Abs(LSPR)}/\text{Abs(450nm)})}$$

AuNPs were also characterized by DLS, and Zeta potential as described in section **2.4.2** to analyze the hydrodynamic diameter and surface charge of particles. DLS and Zeta potential data analysis (**Table 3.1**) revealed that the AuNPs presented a hydrodynamic diameter of 19nm and a surface charge of -54mV, as citrate capping confers a negative charge to the particles[103].

AuNP characterization indicated that the synthesized particles had the expected size, were rather stable in the colloidal solution and thus ready to use for functionalization with PEG-COOH.

3.1.2 Characterization of AuNP@PEG-COOH

The AuNPs were then functionalized with PEG-COOH to achieve 100% surface coverage as described in section **2.2.1**, to increase particle stability and more importantly to allow for further functionalization with any molecule harboring a free amine group.

Following functionalization AuNP@PEG-COOH were characterized through U.V-visible spectrophotometry as described in section **2.4.1**. to observe the LSPR peak and determine particle concentration. A spectrum of the AuNP@PEG-COOH was obtained (**Figure 3.1**), where the LSPR peak was observed at 520nm (**Table 3.1**), then particle concentration determined through the lambert-Beer law at 57nM. The red-shift in the LSPR peak from 519nm to 520nm after PEG-COOH functionalization is an indicator of particle size increase pointing towards a success in AuNP functionalization with PEG-COOH.[104]

AuNP@PEG-COOH were also characterized by DLS, and Zeta potential as described in section **2.4.2** to analyze the hydrodynamic diameter and surface charge of particles. DLS and Zeta potential data analysis (**Table 3.1**) revealed that the AuNP@PEG-COOH presented a hydrodynamic diameter of 25nm and a surface charge of -47mV.

DLS data comparison corroborates with the increase in particle size observed through the red-shift in AuNP@PEG-COOH spectrum as the particle hydrodynamic diameter increased from 19nm to 25nm after functionalization. Zeta potential data comparison also points toward successful functionalization since surface charge became less negative from -54mV to -47mV. The particle surface charge becoming slightly less negative may be attributed to the citrate capping being removed and replaced with PEG-COOH[103].

To further confirm that particle functionalization with PEG-COOH was successful, Ellman's assay was performed as described in section **2.2.2** to determine the concentration of free PEG-COOH chains, obtained after particle functionalization (see section **2.2.1**). Free PEG-COOH chain concentration was determined through **Equation 3.2** at 0,00057343 mg/ml resulting in a 95.01% reaction yield regarding AuNP functionalization with PEG-COOH.

Equation 3.2:

$$Abs_{412} = 8.0219x[PEG\text{-}COOH] - 0.0066$$

AuNP@PEG-COOH characterization and Ellman's assay point towards a successful synthesis of stable PEG-COOH covered AuNP@PEG-COOH ready to use for Anti-LAMP2A functionalization.

3.1.3 Characterization of AuNP@PEG-COOH@Anti-LAMP2A

Lastly, through the EDC/NHS coupling reaction AuNP@PEG-COOH were functionalized with an Anti-LAMP2A antibody to achieve a maximum surface coverage of ten antibody molecules per nanoparticle (see **Figure A2** in **annex A**) as described in section **2.3.1** for an active targeting of the lysosomal associated membrane protein 2A (LAMP2A).

Following functionalization AuNP@PEG-COOH@Anti-LAMP2A were characterized through U.V-visible spectrophotometry as described in section **2.4.1**. to observe the LSPR peak and determine particle concentration. A spectrum of the AuNP@PEG-COOH was obtained (**Figure 3.1**), the LSPR peak was observed at 544nm (**Table 3.1**), then particle concentration determined through the lambert-Beer law at 26nM. The red-shift in the LSPR peak from 520nm to 544nm after Anti-LAMP2A functionalization is an indicator of particle size increase, pointing towards a success in AuNP@PEG-COOH functionalization with Anti-LAMP2A [104]

To further confirm the success of AuNP@PEG-COOH functionalization with Anti-LAMP2A, Bradford assay was performed as described in section **2.3.2** to determine the concentration of free Anti-LAMP2A antibodies, obtained after particle functionalization (see section **2.3.1**). Free Anti-LAMP2A concentration was determined through **Equation 3.3** at 11.94µg/mL resulting in a 60.1% yield regarding AuNP@PEG-COOH functionalization with Anti-LAMP2A.

Equation 3.3

$$Abs_{595nm} = 0.008x[Anti\text{-}LAMP2A] + 0.002$$

AuNP@PEG-COOH@Anti-LAMP2A characterization and Bradford assay point towards a successful synthesis of synthesis of Anti-LAMP2A functionalized AuNP@PEG-COOH ready to be used as a photothermal agent for specific targeting of the lysosomes.

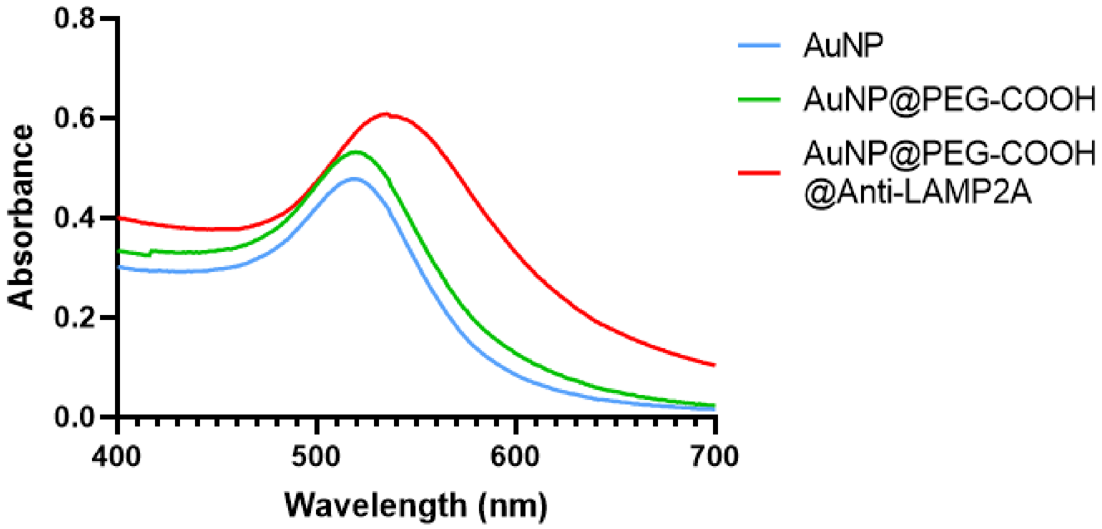

Figure 3.1- *Obtained spectra of citrate capped gold nanoparticles (AuNP), PEG-COOH functionalized AuNPs (AuNP@PEG-COOH) and Anti-LAMP2A functionalized AuNP@PEG-COOH (AuNP@PEG-COOH@Anti-LAMP2A). Through the observation of these spectra, it is possible to distinguish a shift in the localized surface plasmon resonance (LSPR) peak indicating a possible increase in particle size after each functionalization.*

Table 3.1: *Gold nanoparticle characterization through UV-Visible Spectrophotometry, Dynamic Light Scattering and Zeta potential.*

UV-Visible Spectrophotometry (Surface Plasmon Resonance peak (nm))	
Citrate capped AuNP	519
AuNP@PEG-COOH	520
AuNP@PEG-COOH@Anti-LAMP2A	544
Dynamic Light Scattering (Particle Hydrodynamic size (diameter nm))	
Citrate capped AuNP	19
AuNP@PEG-COOH	25
Zeta Potential (mV)	
Citrate capped AuNP	-54
AuNP@PEG-COOH	-47

In the first part of this work, Citrate capped AuNPs with 14nm were synthesized, their surface covered with PEG-COOH (AuNP@PEG-COOH) and functionalized with Anti-LAMP2A antibody successfully obtaining AuNP@PEG-COOH@Anti-LAMP2A for cell challenging and lysosomal disruption though photothermal assay. A work scheme of this study is represented in **Figure 3.2**

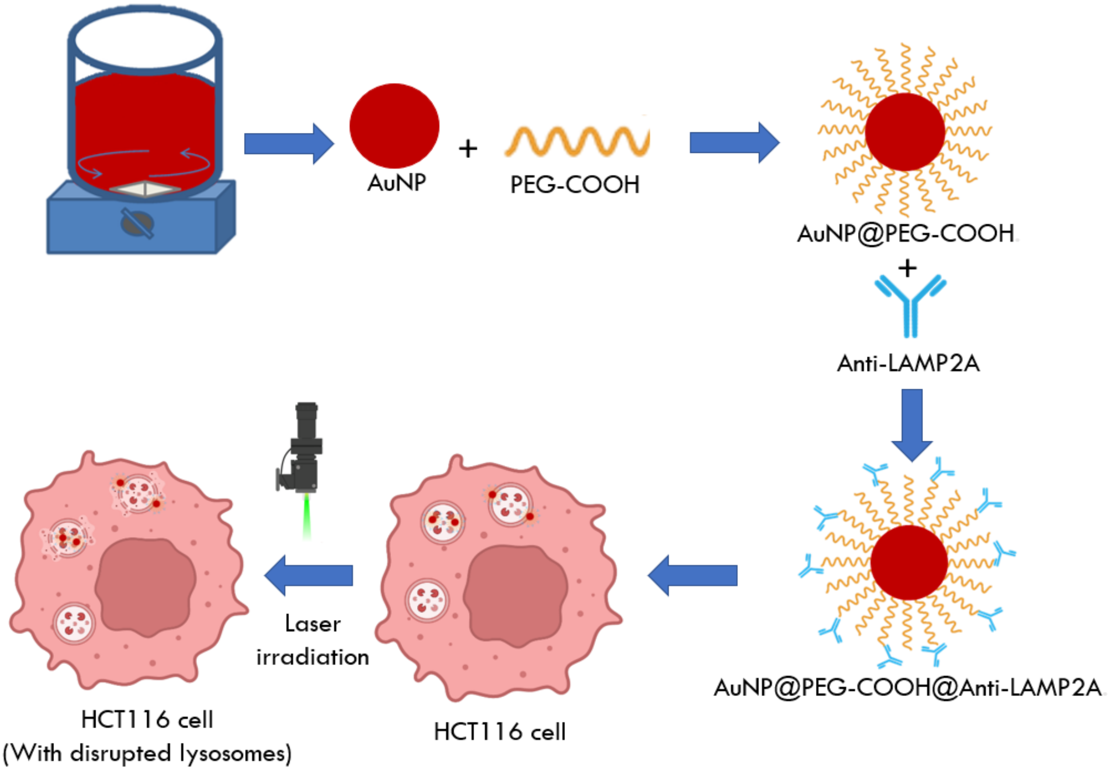

Figure 3.2- ***Work scheme representing the several steps of lab work.*** *Starting from the synthesis of AuNPs followed by conjugation with PEG-COOH and functionalization with Anti-LAMP2A (AuNP@PEG-COOH@Anti-LAMP2A) and leading to the irradiation of nanoparticle incubated HCT116 cells for lysosomal targeting and disruption through photothermal assay.*

3.2 Challenging of cells with Au-nanoconjugates

HCT116 cell challenging was performed with the AuNP@PEG-COOH and AuNP@PEG-COOH@Anti-LAMP2A as described in section **2.6** to study cellular uptake, lysosomal targeting, and the effect on cell viability.

3.2.1 Uptake of Gold Nanoparticles

U.V-visible spectrophotometry was performed as described in section **2.6.1** to determine the intracellular concentration of nanoparticles after a 24h incubation with HCT116 cells. As shown in **Figure 3.3** AuNP@PEG-COOH@Anti-LAMP2A have a much higher cellular concentration than AuNP@PEG-COOH, with 63% particle uptake and 12.2% particle uptake respectively, meaning that functionalization with Anti-LAMP2A leads to a much higher cellular uptake of the AuNP@PEG-COOH@Anti-LAMP2A.

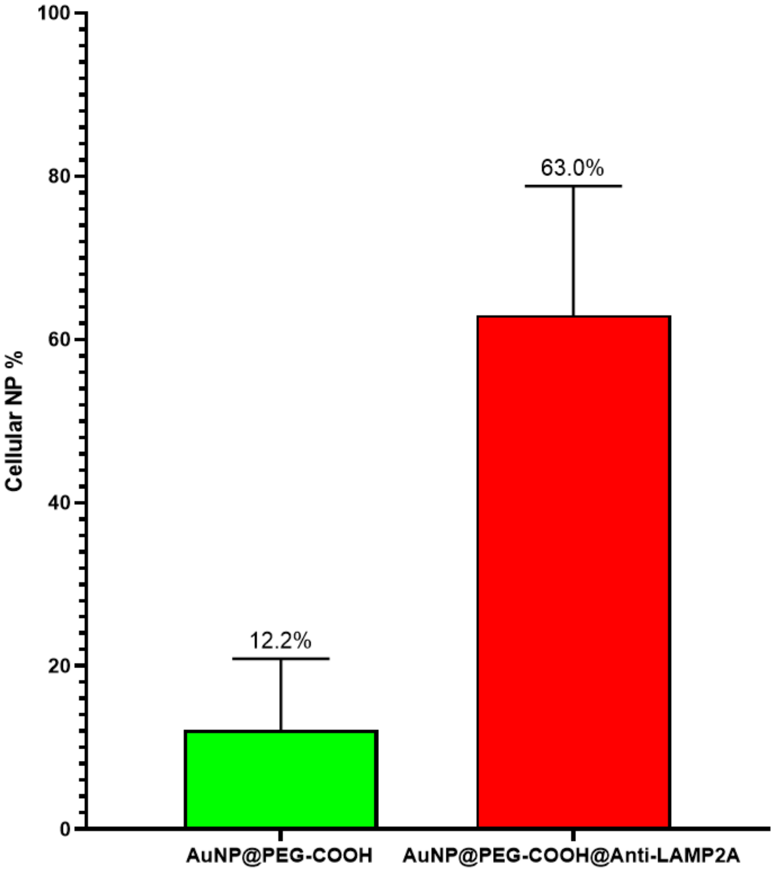

Figure 3.3- ***Gold nanoparticle uptake by HCT116 cells after 24 hours of incubation.*** *Only 12.2% of PEG-COOH covered gold nanoparticles (AuNP@PEG-COOH) are incorporated by the cells whereas 63% of Anti-LAMP2A functionalized gold nanoparticles (AuNP@PEG-COOH@Anti-LAMP2A) are incorporated meaning that Anti-LAMP2A functionalization leads to a higher cellular uptake.*

3.2.2 Intracellular accumulation of Gold Nanoparticles

In section **3.2.1** AuNP@PEG-COOH@Anti-LAMP2A were shown to have a much higher cellular uptake than AuNP@PEG-COOH proving that these particles are present inside the cells after a 24h incubation but its location is unknow. Since the active targeting of the lysosomes is of great importance in this study, inductively coupled plasma atomic emission spectroscopy (ICP-AES) an analytical technique capable of detecting trace amounts of metallic elements in samples, was performed to determine the cellular location of the AuNP@PEG-COOH.

To that end, cell challenge and fractionation were performed as described in section **2.6.2** and fractionated samples prepared for ICP-AES analysis as described in section **2.6.3.** Gold concentration in each sample was determined considering the initial gold concentration added to each well, subtracted by gold concentration detected and quantified by ICP-AES **(Table 3.2).** The sum of AuNP@PEG-COOH@Anti-LAMP2A percentages in **Table 3.2** does not reach 100%, because during fractionation and ICP-AES sample preparation some AuNP@PEG-COOH@Anti-LAMP2A precipitated and were lost in the washing steps. Nevertheless ICP-AES data analysis of the cellular fractions **Table 3.2** revealed that AuNP@PEG-COOH were not incorporated or absorbed to the cellular membrane while AuNP@PEG-COOH@Anti-LAMP2A seem to have a preferential accumulation in the nucleus which is unexpected given the fact that the lysosomes are present in the cytosolic fraction. The reason for this, could be because there is an accumulation of the particles in the lysosomes, ultimately leading to an increase in density and since the different cellular fractions were separated by differential precipitation according to density, the cytosolic fraction having the lowest density and the nuclear the highest, the particle filled lysosomes might have precipitated along with the nuclear fraction. Nevertheless, as also seen in section **3.2.1** AuNP@PEG-COOH@Anti-LAMP2A do seem to have increased cell uptake by HCT116 cells in comparison to the AuNP@PEG-COOH, further proving that particle functionalization with Anti-LAMP2A results in an increased cellular uptake with a preferential accumulation in the nuclear fraction.

Table 3.2: ***Gold concentration detected through ICP-AES in cellular fractions.*** *Obtained from HCT116 cells incubated with AuNP@PEG-COOH and AuNP@PEG-COOH@Anti-LAMP2A for 24 h.*

	AuNP@PEG-COOH	AuNP@PEG-COOH@Anti-LAMP2A
Supernatant	110%	52%
Cytosolic fraction	0%	0%
Mitochondrial fraction	0%	1%
Nuclear fraction	0%	18%

3.2.3 Lysosome presence in the cellular fractions

In section **3.2.1** AuNP@PEG-COOH@Anti-LAMP2A showed a high cellular uptake and in section **3.2.2** through ICP-AES analysis, these particles seemed to have a preferential accumulation in the nuclear fraction, rather than the cytosolic fraction where lysosomes are usually present. However, that might be due to an increase in lysosomal density, as a consequence of AuNP@PEG-COOH@Anti-LAMP2A accumulation, resulting in lysosomal precipitation with the nuclear fraction.

To verify this hypothesis, western blot analysis was performed to determine if "particle filled" lysosomes were in the nuclear fraction thus indicating that AuNP@PEG-COOH functionalization with Anti-LAMP2A leads to an active targeting of the lysosomes. The target for western blot analysis was the lysosome associated membrane protein 2A (LAMP2A) since the AuNP@PEG-COOH@Anti-LAMP2A were functionalized with an antibody that targets this specific protein. Studies have shown that LAMP2A monomers have molecular weights between 90-120KDa [105,106]

Cell challenge and fractionation was performed as described in section **2.6.2** with the exception that only AuNP@PEG-COOH@Anti-LAMP2A were used, and protein concentration of the cellular fractions quantified by pierce assay as described in section **2.8.1**. Cellular fraction samples were prepared as described in section **2.8.2** and SDS-PAGE electrophoresis was performed followed by membrane transfer as described in section **2.8.3**. Membranes were blocked and antibody staining was performed as described in section **2.8.4** followed by film exposure as described in section **2.8.5**. For western blot analysis the membrane containing the control samples will be referred to as control membrane and the membrane containing the cellular fractions of HCT116 cells incubated with the nanoparticles will be referred to as the study membrane.

Before analyzing in detail, the resulting images of the western blots, one must take an overall view of the process (**Figures 3.4** and **3.5**). Despite great efforts to optimize the blotting and the detection procedure, there were some issues relating to unspecific anti-body binding and absence of β-actin control, which will be discussed in detail when assessing each individual scenario.

Firstly, membranes were stained only with the secondary antibody, Cell Signaling anti-rabbit IgG, HRP-linked Antibody #7074, to mark the Anti-LAMP2A antibody that was functionalized in the AuNP@PEG-COOH@Anti-LAMP2A to determine their presence in the cellular fractions. After film exposure, as expected no bands were detected in the control membrane **Figure 3.4a** because cells were not incubated with the AuNP@PEG-COOH@Anti-LAMP2A meaning that there are no primary antibodies for the secondary antibody to target. Regarding the study membrane **Figure 3.4b** bands with a size of approximately 90 KDa were observed in the mitochondrial and nuclear fractions and no bands were observed in the cytosolic fraction meaning that the AuNP@PEG-COOH@Anti-LAMP2A were present in these two fractions as was also seen in the ICP-AES analysis, where traces of gold were detected in both fractions with a preferential accumulation in the nuclear fraction (see section **3.2.2**).

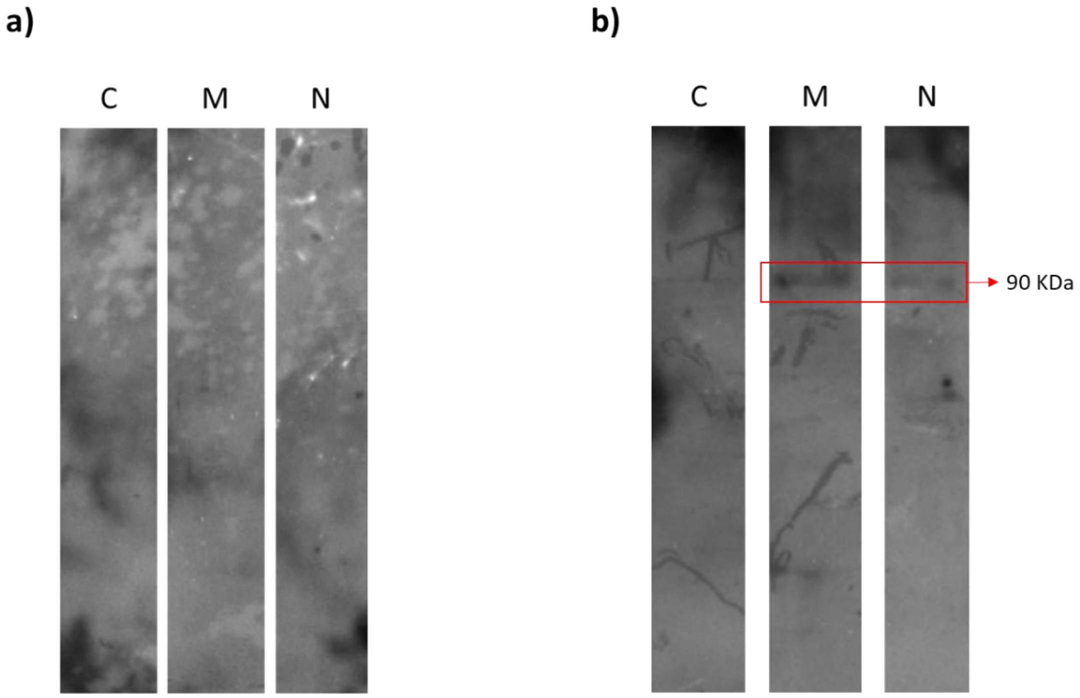

Figure 3.4-***Representative images of western blot analysis of membranes stained only with the secondary antibody, Goat Anti-Rabbit IgG H&L (HRP) (ab205718) a)*** *Control HCT116 cellular fractions;* ***b)*** *Cellular fractions of HCT116 cells incubated with AuNP@PEG-COOH@Anti-LAMP2A for 24 h. C-Cytosolic fraction; M-Mitochondrial fraction; N-Nuclear fraction.*

The membranes were then Stripped as described in section **2.8.6**, followed by blocking, primary and secondary antibody staining as described in section **2.8.4** to stain all the lysosomes in the cellular fractions and not only those that might have incorporated the AuNP@PEG-COOH@Anti-LAMP2A. After film exposure several identic bands **(Figures 3.5a and 3.5b)** between the cytosolic fraction of the control membrane and the study membrane were observed. The same is also true for the mitochondrial fractions between the two membranes. These bands could be the result of unspecific primary antibody binding due to the use of the SDS loading buffer supplied in the fractionation kit. In the control membrane **(Figure 3.5a)**, due to the many bands, in the cytosolic and mitochondrial fractions it is hard to distinguish the approximately 100KDa bands that may correspond to LAMP2A in each. However, no bands were observed in the nuclear fraction meaning that LAMP2A is absent in this fraction as expected. Regarding the study membrane **(Figure 3.5b)**, as with the control membrane the bands corresponding to LAMP2A in the cytosolic and mitochondrial fractions are hard to distinguish, but there is the presence of an approximately 100KDa band in the nuclear fraction, proving the presence of LAMP2A in this fraction as hypothesized.

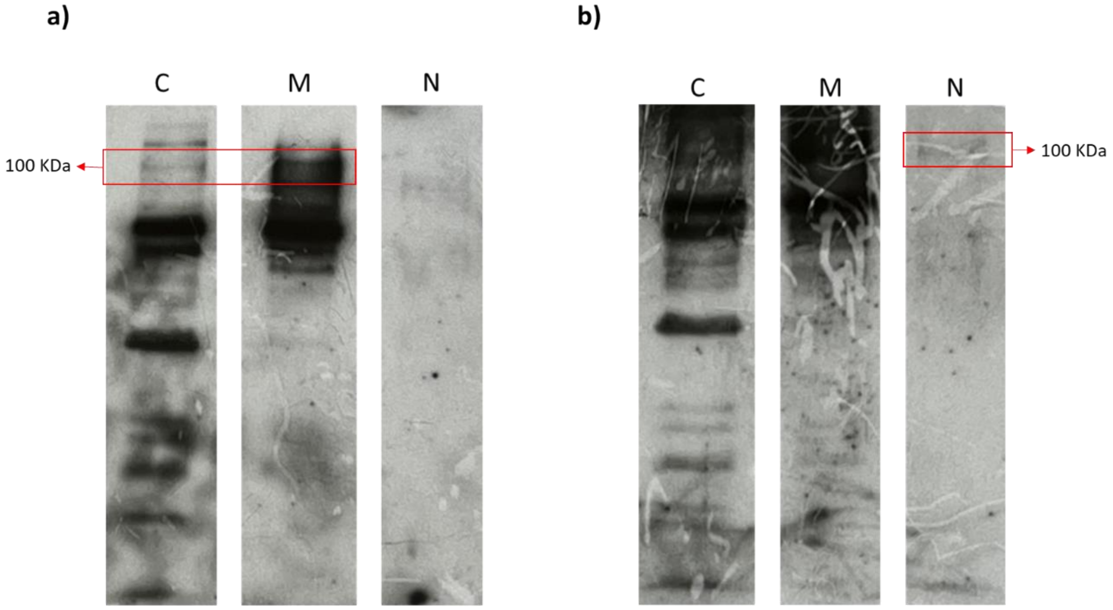

Figure 3.5- ***Representative images of western blot analysis of membranes stained with the primary antibody, Anti-LAMP2A antibody [EPR4207(2)]- Lysosome Marker (ab125068) and secondary antibody, Goat Anti-Rabbit IgG H&L (HRP) (ab205718) a)*** *Control HCT116 cellular fractions;* ***b)*** *Cellular fractions of HCT116 cells incubated with AuNP@PEG-COOH@Anti-LAMP2A for 24 h. C-Cytosolic fraction; M-Mitochondrial fraction; N-Nuclear fraction.*

For actin control, membrane stripping was performed as described in section **2.8.6**, and antibody staining performed as described in section **2.8.7.** However, no bands were observed regarding β-actin control. This could be due to cell fractionation, because in fractionated samples β-actin availability is very low. However western blot analysis was performed simply to determine the presence of lysosomes, through staining of the LAMP2A protein, and AuNP@PEG-COOH@Anti-LAMP2A and not to quantify any levels of expression. For that matter the absence of β-actin bands in this qualitative analysis is of no great concern.

Through western blot data analysis, the presence of "particle filled" lysosomes was confirmed in the nuclear fraction, meaning that AuNP@PEG-COOH functionalization with Anti-LAMP2A leads to a higher cellular uptake and targeting of the lysosomes resulting in a density increase of these organelles.

3.3 Immunofluorescence Microscopy

In section **3.2.1** the presence of AuNP@PEG-COOH@Anti-LAMP2A in the cells was confirmed through U.V-visible spectrophotometry, in section **3.2.2** through ICP-AES analysis particles showed a preferential accumulation in the nuclear fraction and in section **3.2.3**, through western blot analysis the presence of "particle filled" lysosomes in the nuclear fraction was confirmed. As such immunofluorescence microscopy was performed to observe the intracellular location of the AuNP@PEG-COOH@Anti-LAMP2A in HCT116 cells after a 24 h incubation and confirm their accumulation in the lysosomes.

As described in section **2.9** HCT116 cells were grown and incubated with CellLight® Lysosomes-GFP *BacMam 2.0 for 48h, cell challenge performed as described in section **2.6** with the exception that 1nM of AuNP@PEG-COOH and AuNP@PEG-COOH@Anti-LAMP2A were added instead of 2.5nM. The cells were then fixated, blocked, and stained with primary antibody Anti-LAMP2A, secondary antibody Goat anti-rabbit IgG (TRITC) and Hoechst 33258 dye, for further information regarding the controls and study wells see **Figure B2** in **annex B**. Cells were then visualized on the microscope through different filters and the obtained images edited as described in section **2.9**.

Through the obtained images there was a lack of signal regarding lysosome staining (FITC filter) in most conditions **(Figure 3.6a);b);c) and d))**. This could be due to insufucient incubation time with CellLight® Lysosomes-GFP *BacMam 2.0 (C10596) since staining is based on the incorporation of an insect virus (baculovirus) containing the mamalian promoter for the expression of a lysosome-GFP fusion peptide. As such a higher incubation period might be necessary in order to obtain a stronger signal. A very weak signal was also observed in AuNP@PEG-COOH@Anti-LAMP2A staining with secondary antibody Goat anti-rabbit IgG (TRITC) (ab6718) (G2A filter) **Figure 3.6b)**. The weakness of the signal could be related be related to the high dilution of the secondary antibody (1:1000) because the presence of the nanoparticles was confirmed by brightfield images (brightfield) **Figure 3.6b)**. Primary and secondary antibody staining images **Figure 3.6c)** showed a weak signal that can also be due to the high dilution of the secondary antibody. As expected there was no signal detected in AuNP@PEG-COOH staining with secondary antibody Goat anti-rabbit IgG (TRITC) (ab6718) (G2A filter) **Figure 3.6d)** due to the absence of the primary antibody Anti-LAMP2A, proving that TRITC signal acquisition with the G2A filter can only be obtained in the presence of the primary antibody, as is the case with the AuNP@PEG-COOH@Anti-LAMP2A.

In order to obtain clearer data in immunofluorescence microscopy analysis, protocol must be optimized with longer incubation times regarding lysosome staining with CellLight® Lysosomes-GFP *BacMam 2.0 (C10596) and lower secondary antibody dilutions.

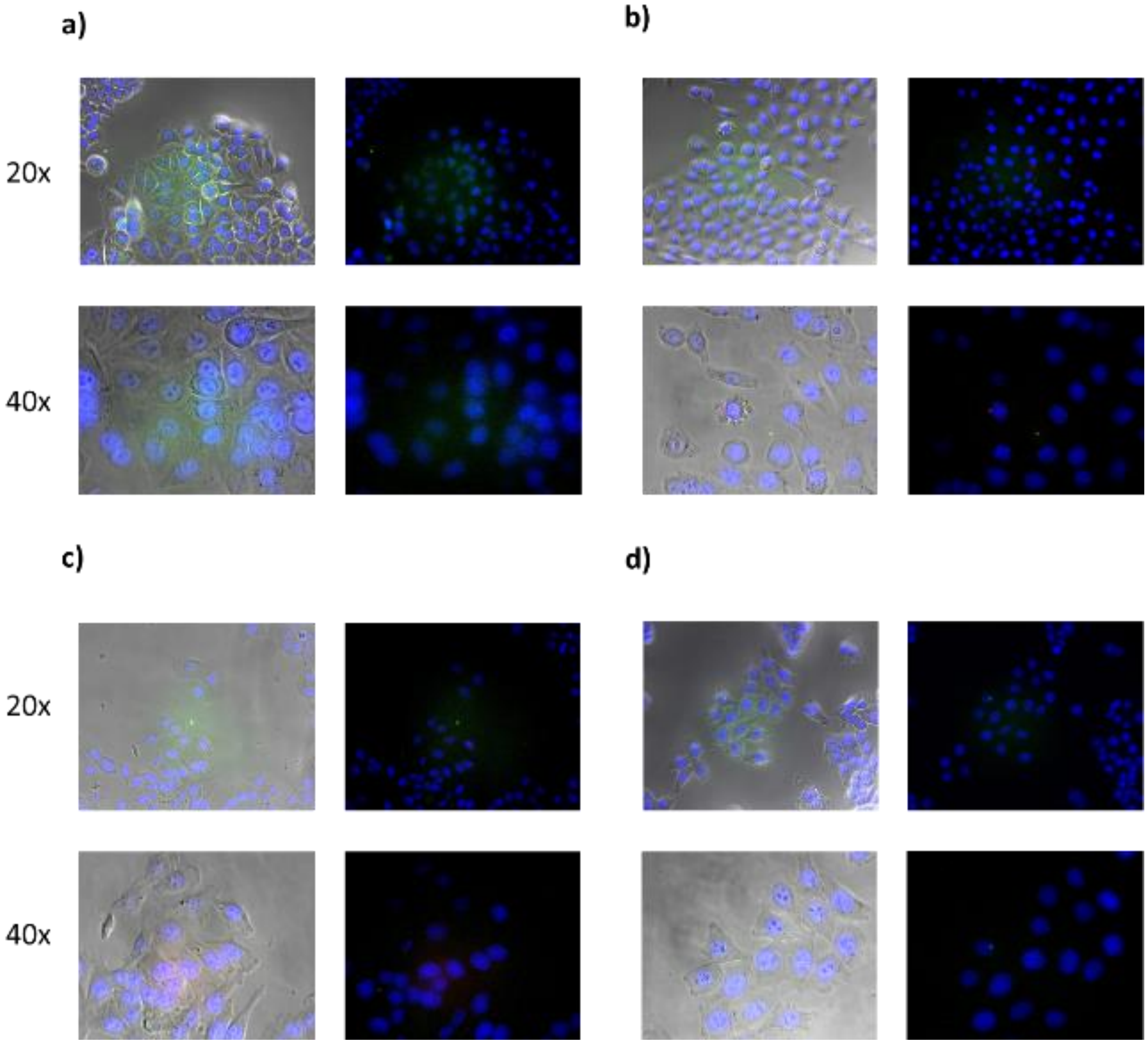

Figure 3.6- ***Bright field and DAPI, FITC, G2A fluorescent images.*** *HCT116 cells stained with CellLight® Lysosomes-GFP *BacMam 2.0 (C10596) and Hoechst 33258* ***a)*** *Cell control;* ***b)*** *24h incubation with AuNP@PEG-COOH@Anti-LAMP2A and secondary antibody Goat anti-rabbit IgG (TRITC) (ab6718) staining;* ***c)*** *Primary antibody Anti-LAMP2A [EPR4207(2)]- Lysosome Marker (ab125068) and secondary antibody Goat anti-rabbit IgG (TRITC) (ab6718) staining;* ***d)*** *24h incubation with AuNP@PEG-COOH and secondary antibody Goat anti-rabbit IgG (TRITC) (ab6718) staining.*

3.4 Photothermy

To determine the potential of AuNP@PEG-COOH@Anti-LAMP2A as a photothermal agent and test their ability to promote cell death or to disrupt cell growth through heat generation photothermy challenge was performed. As described in section **2.10** cell challenge was performed, the cells irradiated with a laser, temperatures taken before and after irradiation and cell viability assessed.

Temperature measurements **Table 3.3**, show no significant temperature increase regarding control wells (1, 2 and 3) after laser irradiation as expected. There was an unexpected temperature increase in control well (4), which could be caused by the presence of precipitated nanoparticles in the bottom of the well that were not completely removed in the washing step. A significant temperature increase was detected in cells incubated with AuNP@PEG-COOH (5) and AuNP@PEG-COOH@Anti-LAMP2A (6) with the latter causing a higher temperature increase, given the fact that more AuNP@PEG-COOH@Anti-LAMP2A were in the cells than AuNP@PEG-COOH as seen before with cellular AuNP quantification (**Figure 3.3**), proving that functionalization with Anti-LAMP2A leads to an higher cellular uptake and consequently to a higher temperature increase after laser irradiation.

Table 3.3: ***Temperature measurements before and after laser irradiation.*** *T_0- Temperature before laser irradiation; T- Temperature after laser irradiation; 1- Phenol red free DMEM Medium only; 2- HCT116 cell control; 3- AuNP@PEG-COOH in Phenol red free DMEM medium; 4- AuNP@PEG-COOH@Anti-LAMP2A in Phenol red free DMEM medium; 5- HCT116 cells incubated with AuNP@PEG-COOH for 24 h; 6- HCT116 cells incubated with AuNP@PEG-COOH@Anti-LAMP2A for 24 h*

	T_0 (ºC)	T (ºC)	ΔT (ºC)
1	35.6	35.7	0.05
2	35.7	36.6	0.9
3	35.6	36.6	1
4	35.6	40.0	4.4
5	35.9	38.7	2.8
6	36.3	46.1	9.8

To verify if laser irradiation of HCT116 cells challenged with AuNP@PEG-COOH and AuNP@PEG-COOH@Anti-LAMP2A had any lead to the promotion of cell death or caused any growth impairment, cell viability was accessed through MTS assay as described in section **2.7.1**. It should be noted that MTS alone does not indicate cell viability but rather mitochondria activity, which in turn may be used as an indirect indicator of the metabolic viability of the cells. MTS assay data analysis **Table 3.4** revealed no significant alteration in cell viability after laser irradiation. Cell viability before and after laser irradiation with AuNP@PEG-COOH and AuNP@PEG-COOH@Anti-LAMP2A showed very similar values with 100% and 95% viability respectively. Cell viability Comparison between irradiated AuNP@PEG-COOH and irradiated AuNP@PEG-COOH@Anti-LAMP2A revealed a 95% viability, meaning that there is almost no difference in cell viability if irradiated HCT116 cells are incubated with AuNP@PEG-COOH or AuNP@PEG-COOH@Anti-LAMP2A, even though the latter has a higher cellular uptake as seen in sections **3.2.1** and **3.2.2**. Cell viability Comparison between non-irradiated AuNP@PEG-COOH and non-irradiated AuNP@PEG-COOH@Anti-LAMP2A revealed a 100% viability, meaning that the incorporation or membrane adsorption of nanoparticles by itself does not affect cell viability. Cell viability before and after laser irradiation of cell control was higher than 100%, meaning that laser irradiation alone does not affect cell viability. This data indicates that nanoparticle irradiation does not immediately promote cell death or any disruption in growth of HCT116 cells through heat generation.

Table 3.4: ***MTS assay.*** *Cell viability comparison before and after 1 min irradiation with 2.37W/cm^2, using a continuous 532 nm green diode-pumped solid-state laser, of HCT116 cells incubated for 24h with 2.5 nM AuNP@PEG-COOH and 2.5 nM AuNP@PEG-COOH@Anti-LAMP2A. Data normalized against the control (irradiated/non-irradiated HCT116 cells without nanoparticles).*

***- Cell viability comparison between irradiated AuNP@PEG-COOH and AuNP@PEG-COOH@Anti-LAMP2A*

***- Cell viability comparison between non-irradiated AuNP@PEG-COOH and AuNP@PEG-COOH@Anti-LAMP2A*

AuNP@PEG-COOH	AuNP@PEG-COOH@Anti-LAMP2A	Irradiated*	Non-irradiated**	Cell control
100%	95%	95%	100%	104%

To verify if laser irradiation of HCT116 cells challenged with AuNP@PEG-COOH and AuNP@PEG-COOH@Anti-LAMP2A had caused any disruptions of the cellular membrane trypan blue exclusion method was performed as described in section **2.7.2** to determine the percentage of living cells.

Trypan blue exclusion method data analysis revealed similar results to the MTS assay. Cell viability before and after laser irradiation with AuNP@PEG-COOH and AuNP@PEG-COOH@Anti-LAMP2A showed very similar values with 101% and 105% viability respectively. Cell viability Comparison between irradiated AuNP@PEG-COOH and irradiated AuNP@PEG-COOH@Anti-LAMP2A revealed a 102% viability, meaning that there is almost no difference in cell viability if irradiated HCT116 cells are incubated with AuNP@PEG-COOH or AuNP@PEG-COOH@Anti-LAMP2A, even though the latter has a higher cellular uptake as seen in sections **3.2.1** and **3.2.2**. Cell viability Comparison between non-irradiated AuNP@PEG-COOH and non-irradiated AuNP@PEG-COOH@Anti-LAMP2A revealed a 98% viability, meaning that the incorporation or membrane adsorption of nanoparticles by itself does not affect cell viability. Cell viability before and after laser irradiation of cell control was higher than 110%, meaning that laser irradiation alone does not affect cell viability. As was also seen through MTS assay this data indicates that nanoparticle irradiation does not immediately promote cell death or any disruption in growth of HCT116 cells through heat generation. Further study is required to verify if laser irradiation of HCT116 cells challenged with nanoparticles can promote cell death or disrupt cellular growth by testing the effect on cell viability with higher nanoparticle concentrations, higher laser potencies and longer irradiation periods.

4

CONCLUSIONS AND FUTURE PERSPECTIVES

The present work evaluated the internalization and accumulation of synthesized gold nanoparticles functionalized with specific antibodies towards recognition of lysosome associated membrane protein 2A (LAMP2A) in the lysosomes of colorectal cancer cell lines and tested their effects as photothermal agents in cell viability and organelle integrity in mild photothermy conditions.

In this work, AuNPs were used for targeting lysosomes and photoirradiation studies in HCT116 cells. Citrate capped AuNPs with 14nm were synthesized, their surface completely covered with PEG-COOH, increasing their stability, biocompatibility and allowing for further functionalization with Anti-LAMP2A for specific targeting of lysosome membrane associated protein 2A (LAMP2A). AuNP characterization showed that each functionalization was successful and stable AuNP@PEG-COOH@Anti-LAMP2A were obtained. HCT116 cells were then challenged for 24h with the AuNP@PEG-COOH@Anti-LAMP2A. Cellular uptake and AuNP@PEG-COOH@Anti-LAMP2A accumulation in the lysosomes was studied through U.V-visible spectroscopy, inductively coupled plasma atomic emission spectroscopy (ICP-AES) and analyzed through western blot, revealing that AuNP@PEG-COOH@Anti-LAMP2A not only showed a high cellular uptake but also had a preferential accumulation in the lysosomes. Attempts to obtain live images of AuNP@PEG-COOH@Anti-LAMP2A through immunofluorescence microscopy were done but resulting images lacked quality and as such the protocol still requires further optimization.

Having confirmed AuNP@PEG-COOH@Anti-LAMP2A accumulation in the lysosomes photothermal assays were performed. Challenged cells were irradiated with a laser, temperatures before and after measured, to quantify the heat generation of the AuNP@PEG-COOH@Anti-LAMP2A, cell viability assessed through MTS assay and membrane integrity assessed through trypan blue exclusion method. Photothermal assay results indicated that no cell death nor membrane disruptions were detected meaning that the AuNP@PEG-COOH@Anti-LAMP2A, when irradiated with the chosen potency and at the concentration chosen for cell challenging caused no major alterations on HCT116 cells, apart from an increase in temperature.

The present study reports a successful targeting of the lysosomes in HCT116 cells through surface modification with PEG-COOH and Anti-LAMP2A antibody functionalization of citrate capped AuNPs. Photothermal assays with the AuNPs were performed in HCT116cells but no critical alterations were observed. Future studies regarding the potential of these AuNP@PEG-COOH@Anti-LAMP2A as photothermal agents are of the utmost importance for their implementation in vivo and further down the line in situ studies for photothermal therapy. Furthermore in vivo and in situ studies still need to be performed before the real impact of these strategies may leave the bench and be suitable for clinical translation.

REFERENCES

1. Bray, F., Laversanne, M., Weiderpass, E. & Soerjomataram, I. The ever-increasing importance of cancer as a leading cause of premature death worldwide. *Cancer* **127**, 3029–3030 (2021).
2. Sung, H. *et al.* Global Cancer Statistics 2020: GLOBOCAN Estimates of Incidence and Mortality Worldwide for 36 Cancers in 185 Countries. *CA. Cancer J. Clin.* **71**, 209–249 (2021).
3. GLOBOCAN. The Global Cancer Observatory - All cancers. *Int. Agency Res. Cancer - WHO* **419**, 199–200 (2020).
4. Urruticoechea, A. *et al.* Recent Advances in Cancer Therapy: An Overview. *Curr. Pharm. Des.* **16**, 3–10 (2010).
5. Phung, D. C. *et al.* Combined hyperthermia and chemotherapy as a synergistic anticancer treatment. *J. Pharm. Investig.* **49**, 519–526 (2019).
6. Hanahan, D. & Weinberg, R. A. Hallmarks of cancer: The next generation. *Cell* **144**, 646–674 (2011).
7. Bertram, J. S. The molecular biology of cancer. *Mol. Aspects Med.* **21**, 167–223 (2000).
8. Kontomanolis, E. N. *et al.* Role of oncogenes and tumor-suppressor genes in carcinogenesis: A review. *Anticancer Res.* **40**, 6009–6015 (2020).
9. Hassanpour, S. H. & Dehghani, M. Review of cancer from perspective of molecular. *J. Cancer Res. Pract.* **4**, 127–129 (2017).
10. Hanahan, D. Hallmarks of Cancer: New Dimensions. *Cancer Discov.* **12**, 31–46 (2022).
11. Hanahan, D. & Weinberg, R. A. The Hallmarks of Cancer. *Cell* **100**, 57–70 (2000).
12. Barker, N. *et al.* Crypt stem cells as the cells-of-origin of intestinal cancer. *Nature* **457**, 608–611 (2009).
13. Perekatt, A. O. *et al.* SMAD4 suppresses WNt-driven dedifferentiation and oncogenesis in the differentiated gut epithelium. *Cancer Res.* **78**, 4878–4890 (2018).
14. Huang, S. Tumor progression: Chance and necessity in Darwinian and Lamarckian somatic (mutationless) evolution. *Prog. Biophys. Mol. Biol.* **110**, 69–86 (2012).
15. Dzutsev, A. *et al.* Microbes and cancer. *Annu. Rev. Immunol.* **35**, 199–228 (2017).
16. Helmink, B. A., Khan, M. A. W., Hermann, A., Gopalakrishnan, V. & Wargo, J. A. The microbiome, cancer, and cancer therapy. *Nat. Med.* **25**, 377–388 (2019).
17. Baker, D. J. *et al.* Naturally occurring p16 Ink4a-positive cells shorten healthy lifespan. *Nature* **530**, 184–189 (2016).
18. Mármol, I., Sánchez-de-Diego, C., Dieste, A. P., Cerrada, E. & Yoldi, M. J. R. Colorectal

carcinoma: A general overview and future perspectives in colorectal cancer. *Int. J. Mol. Sci.* **18**, (2017).

19. Fearon, E. R. Molecular genetics of colorectal cancer. *Annu. Rev. Pathol. Mech. Dis.* **6**, 479–507 (2011).
20. Markowitz, S. D. & Bertagnolli, M. M. Molecular Basis of Colorectal Cancer. *N. Engl. J. Med.* **361**, 2449–2460 (2009).
21. Sehgal, R. *et al.* Lynch Syndrome: An updated review. *Genes (Basel).* **5**, 497–507 (2014).
22. Centelles, J. J. General Aspects of Colorectal Cancer. *ISRN Oncol.* **2012**, 1–19 (2012).
23. Saftig, P. & Klumperman, J. Lysosome biogenesis and lysosomal membrane proteins: Trafficking meets function. *Nat. Rev. Mol. Cell Biol.* **10**, 623–635 (2009).
24. Luzio, J. P., Pryor, P. R. & Bright, N. A. Lysosomes: Fusion and function. *Nat. Rev. Mol. Cell Biol.* **8**, 622–632 (2007).
25. Settembre, C., Fraldi, A., Medina, D. L. & Ballabio, A. Signals from the lysosome: A control centre for cellular clearance and energy metabolism. *Nat. Rev. Mol. Cell Biol.* **14**, 283–296 (2013).
26. Mahapatra, K. K. *et al.* The lysosome as an imperative regulator of autophagy and cell death. *Cell. Mol. Life Sci.* **78**, 7435–7449 (2021).
27. Dielschneider, R. F., Henson, E. S. & Gibson, S. B. Lysosomes as Oxidative Targets for Cancer Therapy. *Oxid. Med. Cell. Longev.* **2017**, (2017).
28. Zhitomirsky, B. & Assaraf, Y. G. Lysosomes as mediators of drug resistance in cancer. *Drug Resist. Updat.* **24**, 23–33 (2016).
29. Mizushima, N. Autophagy: Process and function. *Genes Dev.* **21**, 2861–2873 (2007).
30. Mizushima, N. & Komatsu, M. Autophagy: Renovation of cells and tissues. *Cell* **147**, 728–741 (2011).
31. Mizushima, N., Levine, B., Cuervo, A. M. & Klionsky, D. J. Autophagy fights disease through cellular self-digestion. *Nature* **451**, 1069–1075 (2008).
32. Ma, Y., Galluzzi, L., Zitvogel, L. & Kroemer, G. Review Autophagy and Cellular Immune Responses. *Immunity* **39**, 211–227 (2013).
33. Burada, F. *et al.* Autophagy in Colorectal Cancer: An Important Switch from Physiology to Pathology. *World J. Gastrointest. Oncol.* **7**, 271–284 (2015).
34. Mathew, R. *et al.* Autophagy suppresses tumor progression by limiting chromosomal instability. *Genes Dev.* **21**, 1367–1381 (2007).
35. Ávalos, Y. *et al.* Tumor Suppression and Promotion by Autophagy. *Biomed Res. Int.* **2014**, (2014).
36. Naumov, G. N., Folkman, J. & Straume, O. Tumor dormancy due to failure of angiogenesis: Role of the microenvironment. *Clin. Exp. Metastasis* **26**, 51–60 (2009).
37. Degenhardt, K. *et al.* Autophagy promotes tumor cell survival and restricts necrosis, inflammation, and tumorigenesis. *Cancer Cell* **10**, 51–64 (2006).
38. Arruebo, M., Vilaboa, N., Sáez-gutierrez, B. & Lambea, J. Assessment of the Evolution of Cancer Treatment Therapies. 3279–3330 (2011) doi:10.3390/cancers3033279.
39. Qiao, J., Liu, Z. & Fu, Y. Adapting conventional cancer treatment for immunotherapy. *J. Mol. Med.* 489–495 (2016) doi:10.1007/s00109-016-1393-4.
40. Zugazagoitia, J. *et al.* Current Challenges in Cancer Treatment. *Clin. Ther.* **38**, 1551–1566 (2016).
41. Kim, B. Y. S., Rutka, J. T. & Chan, W. C. W. Nanomedicine. *N. Engl. J. Med.* **363**, 2434–2443

(2010).
42. Kim, K. Y. Nanotechnology platforms and physiological challenges for cancer therapeutics. *Nanomedicine Nanotechnology, Biol. Med.* **3**, 103–110 (2007).
43. Chen, H. *et al.* Precise nanomedicine for intelligent therapy of cancer. *Sci. China Chem.* **61**, 1503–1552 (2018).
44. Shi, J., Kantoff, P. W., Wooster, R. & Farokhzad, O. C. Cancer nanomedicine: Progress, challenges and opportunities. *Nat. Rev. Cancer* **17**, 20–37 (2017).
45. Kim, E. M. & Jeong, H. J. Current Status and Future Direction of Nanomedicine: Focus on Advanced Biological and Medical Applications. *Nucl. Med. Mol. Imaging (2010).* **51**, 106–117 (2017).
46. Wicki, A., Witzigmann, D., Balasubramanian, V. & Huwyler, J. Nanomedicine in cancer therapy : Challenges , opportunities , and clinical applications. *J. Control. Release* **200**, 138–157 (2015).
47. Bor, G., Diana, I., Azmi, M. & Yaghmur, A. Nanomedicines for cancer therapy : current status , challenges and future prospects. (2019).
48. Wilczewska, A. Z., Niemirowicz, K., Markiewicz, K. H. & Car, H. Nanoparticles as drug delivery systems. *Pharmacol. Reports* **64**, 1020–1037 (2012).
49. Liu, Y., Miyoshi, H. & Nakamura, M. Nanomedicine for drug delivery and imaging : A promising avenue for cancer therapy and diagnosis using targeted functional nanoparticles. **2537**, 2527–2537 (2007).
50. Chapman, S. *et al.* Nanoparticles for cancer imaging : The good , the bad , and the promise. *Nano Today* **8**, 454–460 (2013).
51. Fang, C. & Zhang, M. Nanoparticle-based theragnostics: Integrating diagnostic and therapeutic potentials in nanomedicine. *J. Control. Release* **146**, 2–5 (2010).
52. Dai, Y., Xu, C., Sun, X. & Chen, X. Nanoparticle design strategies for enhanced anticancer therapy by exploiting the tumour microenvironment. *Chem. Soc. Rev.* **46**, 3830–3852 (2017).
53. Bertrand, N., Wu, J., Xu, X., Kamaly, N. & Farokhzad, O. C. Cancer nanotechnology: The impact of passive and active targeting in the era of modern cancer biology. *Adv. Drug Deliv. Rev.* **66**, 2–25 (2014).
54. Jain, R. K. & Stylianopoulos, T. Delivering nanomedicine to solid tumors. *Nat. Rev. Clin. Oncol.* **7**, 653–664 (2010).
55. Kydd, J. *et al.* Targeting strategies for the combination treatment of cancer using drug delivery systems. *Pharmaceutics* **9**, (2017).
56. Mohd-Zahid, M. H. *et al.* Colorectal cancer stem cells: A review of targeted drug delivery by gold nanoparticles. *RSC Adv.* **10**, 973–985 (2019).
57. Haley, B. & Frenkel, E. Nanoparticles for drug delivery in cancer treatment. *Urol. Oncol. Semin. Orig. Investig.* **26**, 57–64 (2008).
58. Danhier, F., Feron, O. & Préat, V. To exploit the tumor microenvironment: Passive and active tumor targeting of nanocarriers for anti-cancer drug delivery. *J. Control. Release* **148**, 135–146 (2010).
59. Kou, L., Sun, J., Zhai, Y. & He, Z. The endocytosis and intracellular fate of nanomedicines: Implication for rational design. *Asian J. Pharm. Sci.* **8**, 1–10 (2013).
60. Wu, M., Guo, H., Liu, L., Liu, Y. & Xie, L. Size-dependent cellular uptake and localization profiles of silver nanoparticles. *Int. J. Nanomedicine* **14**, 4247–4259 (2019).

61. Zhang, S., Li, J., Lykotrafitis, G., Bao, G. & Suresh, S. Size-dependent endocytosis of nanoparticles. *Adv. Mater.* **21**, 419–424 (2009).
62. Carvalho, A., Fernandes, A. R. & Baptista, P. V. *Chapter 10 - Nanoparticles as Delivery Systems in Cancer Therapy: Focus on Gold Nanoparticles and Drugs. Applications of Targeted Nano Drugs and Delivery Systems* (Elsevier Inc., 2019). doi:10.1016/B978-0-12-814029-1.00010-7.
63. Lopes, T. S., Alves, G. G., Pereira, M. R., Granjeiro, J. M. & Leite, P. E. C. Advances and potential application of gold nanoparticles in nanomedicine. *J. Cell. Biochem.* **120**, 16370–16378 (2019).
64. Yohan, D. & Chithrani, B. D. Applications of nanoparticles in nanomedicine. *J. Biomed. Nanotechnol.* **10**, 2371–2392 (2014).
65. Boisselier, E. & Astruc, D. Gold nanoparticles in nanomedicine: preparations, imaging, diagnostics, therapies and toxicity. *Chem. Soc. Rev.* **38**, 1759–1782 (2009).
66. Turkevich, J., Stevenson, P. C. & Hillier, J. A study of the nucleation and growth processes in the synthesis of colloidal gold. *Discuss. Faraday Soc.* **11**, 55–75 (1951).
67. Duncan, B., Kim, C. & Rotello, V. M. Gold nanoparticle platforms as drug and biomacromolecule delivery systems. *J. Control. Release* **148**, 122–127 (2010).
68. Mieszawska, A. J., Mulder, W. J. M., Fayad, Z. A. & Cormode, D. P. Multifunctional gold nanoparticles for diagnosis and therapy of disease. *Mol. Pharm.* **10**, 831–847 (2013).
69. Mock, J. J. *et al.* Distance-dependent plasmon resonant coupling between a gold nanoparticle and gold film. *Nano Lett.* **8**, 2245–2252 (2008).
70. Mustafa, D. E. *et al.* Surface Plasmon Coupling Effect of Gold Nanoparticles with Different Shape and Size on Conventional Surface Plasmon Resonance Signal. *Plasmonics* **5**, 221–231 (2010).
71. Conde, J. *et al.* Revisiting 30 years of biofunctionalization and surface chemistry of inorganic nanoparticles for nanomedicine. *Front. Chem.* **2**, 1–27 (2014).
72. Tiwari, P. M., Vig, K., Dennis, V. A. & Singh, S. R. Functionalized gold nanoparticles and their biomedical applications. *Nanomaterials* **1**, 31–63 (2011).
73. Nicol, J. R., Dixon, D. & Coulter, J. A. Gold nanoparticle surface functionalization: A necessary requirement in the development of novel nanotherapeutics. *Nanomedicine* **10**, 1315–1326 (2015).
74. Soto, K. M., Mendoza, S., López-Romero, J. M., Gasca-Tirado, J. R. & Manzano-Ramírez, A. Gold nanoparticles: synthesis, application in colon cancer therapy and new approaches - review. *Green Chem. Lett. Rev.* **14**, 663–676 (2021).
75. Ghorbani, F., Kokhaei, P., Ghorbani, M. & Eslami, M. Application of different nanoparticles in the diagnosis of colorectal cancer. *Gene Reports* **21**, 100896 (2020).
76. Huang, X., Jain, P. K., El-Sayed, I. H. & El-Sayed, M. A. Plasmonic photothermal therapy (PPTT) using gold nanoparticles. *Lasers Med. Sci.* **23**, 217–228 (2008).
77. Jori, G. & Spikes, J. D. Photothermal sensitizers: Possible use in tumor therapy. *J. Photochem. Photobiol. B Biol.* **6**, 93–101 (1990).
78. Riley, R. S. & Day, E. S. Gold nanoparticle-mediated photothermal therapy: applications and opportunities for multimodal cancer treatment. *Wiley Interdiscip. Rev. Nanomedicine Nanobiotechnology* **9**, (2017).
79. Cheng, Y. *et al.* Highly efficient drug delivery with gold nanoparticle vectors for in vivo photodynamic therapy of cancer. *J. Am. Chem. Soc.* **130**, 10643–10647 (2008).

80. Beik, J. *et al.* Gold nanoparticles in combinatorial cancer therapy strategies. *Coord. Chem. Rev.* **387**, 299–324 (2019).
81. Dykman, L. A. & Khlebtsov, N. G. Gold nanoparticles in chemo-, immuno-, and combined therapy: review [Invited]. *Biomed. Opt. Express* **10**, 3152 (2019).
82. Kundra, R. & Kornfeld, S. Asparagine-linked oligosaccharides protect Lamp-1 and Lamp-2 from intracellular proteolysis. *J. Biol. Chem.* **274**, 31039–31046 (1999).
83. Chen, J. W., Murphy, T. L., Wlllingham, M. C., Pastan, I. & August, J. T. Identification of two lysosomal membrane glycoproteins. *J. Cell Biol.* **101**, 85–95 (1985).
84. Fehrenbacher, N. *et al.* Sensitization to the Lysosomal Cell Death Pathway by Oncogene-Induced Down-regulation of Lysosome-Associated Membrane Proteins 1 and 2. 6623–6633 (2008) doi:10.1158/0008-5472.CAN-08-0463.
85. Boya, P. & Kroemer, G. Lysosomal membrane permeabilization in cell death. 6434–6451 (2008) doi:10.1038/onc.2008.310.
86. Aits, S. & Ja, M. Lysosomal cell death at a glance. (2013) doi:10.1242/jcs.091181.
87. Kroemer, G., Jäättelä, M., Desmoulins, C. & Villejuif, F.-. LYSOSOMES AND AUTOPHAGY IN CELL DEATH CONTROL. **5**, 886–897 (2005).
88. Fernandes, A. R. *et al.* Multifunctional gold-nanoparticles: A nanovectorization tool for the targeted delivery of novel chemotherapeutic agents. *J. Control. Release* **245**, 52–61 (2017).
89. Lee, P. C. & Meisel, D. Adsorption and surface-enhanced Raman of dyes on silver and gold sols. *J. Phys. Chem.* **86**, 3391–3395 (1982).
90. Alex, S. & Tiwari, A. Functionalized gold nanoparticles: Synthesis, properties and applications-A review. *J. Nanosci. Nanotechnol.* **15**, 1869–1894 (2015).
91. Polte, J. *et al.* Mechanism of gold nanoparticle formation in the classical citrate synthesis method derived from coupled in situ XANES and SAXS evaluation. *J. Am. Chem. Soc.* **132**, 1296–1301 (2010).
92. Uz, M., Bulmus, V. & Alsoy Altinkaya, S. Effect of PEG Grafting Density and Hydrodynamic Volume on Gold Nanoparticle-Cell Interactions: An Investigation on Cell Cycle, Apoptosis, and DNA Damage. *Langmuir* **32**, 5997–6009 (2016).
93. Manson, J., Kumar, D., Meenan, B. J. & Dixon, D. Polyethylene glycol functionalized gold nanoparticles: The influence of capping density on stability in various media. *Gold Bull.* **44**, 99–105 (2011).
94. Conde, J., Rosa, J., de la Fuente, J. M. & Baptista, P. V. Gold-nanobeacons for simultaneous gene specific silencing and intracellular tracking of the silencing events. *Biomaterials* **34**, 2516–2523 (2013).
95. Geißler, D., Nirmalananthan-Budau, N., Scholtz, L., Tavernaro, I. & Resch-Genger, U. Analyzing the surface of functional nanomaterials—how to quantify the total and derivatizable number of functional groups and ligands. *Microchim. Acta* **188**, (2021).
96. Xuan, Y., Zhao, S., Xiao, X., Xiang, L. & Zheng, H. C. Inhibition of chaperone-mediated autophagy reduces tumor growth and metastasis and promotes drug sensitivity in colorectal cancer. *Mol. Med. Rep.* **23**, (2021).
97. Bart, J. *et al.* Room-temperature intermediate layer bonding for microfluidic devices. *Lab Chip* **9**, 3481–3488 (2009).
98. Haiss, W., Thanh, N. T. K., Aveyard, J. & Fernig, D. G. Determination of Size and Concentration of Gold Nanoparticles from UV−Vis Spectra. *Anal. Chem.* **79**, 4215–4221

(2007).

99. Stetefeld, J., McKenna, S. A. & Patel, T. R. Dynamic light scattering: a practical guide and applications in biomedical sciences. *Biophys. Rev.* **8**, 409–427 (2016).
100. Bhattacharjee, S. DLS and zeta potential - What they are and what they are not? *J. Control. Release* **235**, 337–351 (2016).
101. Kaszuba, M., Corbett, J., Watson, F. M. N. & Jones, A. High-concentration zeta potential measurements using light-scattering techniques. *Philos. Trans. R. Soc. A Math. Phys. Eng. Sci.* **368**, 4439–4451 (2010).
102. Corporation, P. CellTitre 96 AQueous Non-Radioactive Cell Proliferation Assay. *Teh. Bull.* **313**, 45–45 (2006).
103. Jara-guajardo, P. *et al.* Gold Nanoparticles Mediate Improved Detection of β -amyloid Aggregates by Fluorescence. 1–16 (2020).
104. Pereira, R. H. A., Keijok, W. J., Prado, A. R., de Oliveira, J. P. & Guimarães, M. C. C. Rapid and sensitive detection of ochratoxin A using antibody-conjugated gold nanoparticles based on Localized Surface Plasmon Resonance. *Toxicon* **199**, 139–144 (2021).
105. Hunziker, W. & Geuze, H. J. Walter Hunziker and Hans J. Geuze. *BioEssays* **18**, 379–389 (1996).
106. Bandyopadhyay, U., Kaushik, S., Varticovski, L. & Cuervo, A. M. The Chaperone-Mediated Autophagy Receptor Organizes in Dynamic Protein Complexes at the Lysosomal Membrane. *Mol. Cell. Biol.* **28**, 5747–5763 (2008).

A

ANNEX A

A.1 Ellman's Assay

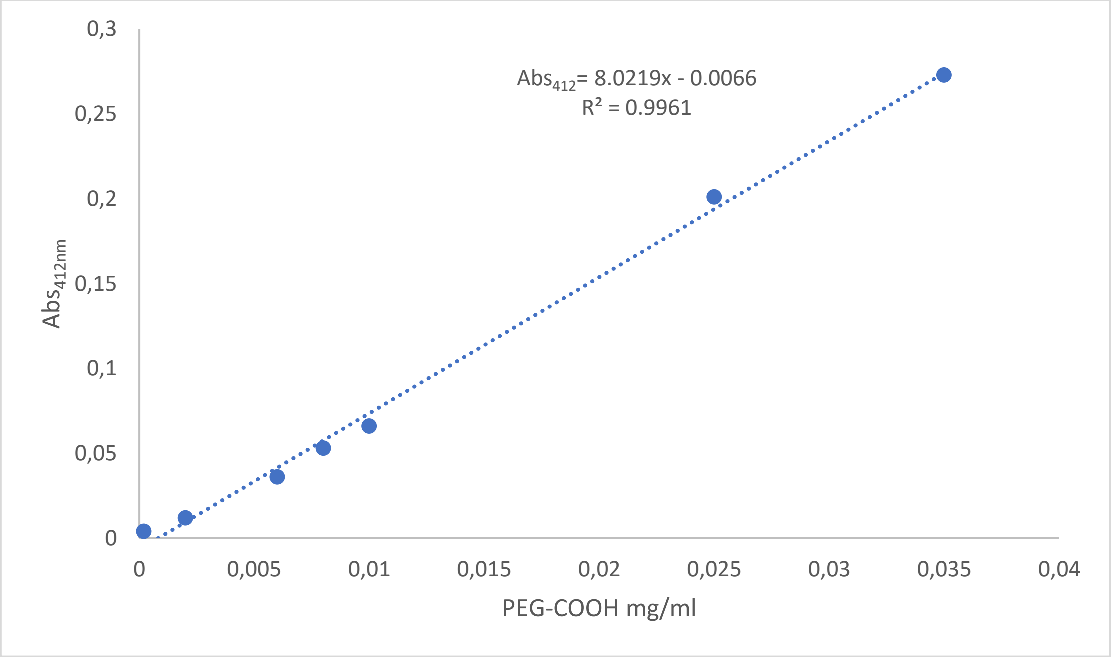

Figure A1 - ***Ellman´s Calibration curve.*** *Obtained through the absorbance reading at 412 nm of prepared PEG-COOH standard solutions ranging from 0.0002-0.035mg/mL previously incubated with DTNB for 10 min, to calculate the concentration of excess PEG-COOH removed after AuNP functionalization, that is correlated to the % of PEG-COOH coverage in the AuNPs.*

A.2 Gold Nanoparticle Anti-LAMP2A Functionalization

By determining the optimal antibody nanoparticle ratio (**Figure A2**) for maximum particle coverage, antibody concentration was determined by considering the amount of gold nanoparticle mols to be functionalized and adding the correspondent ratio of antibody mols.

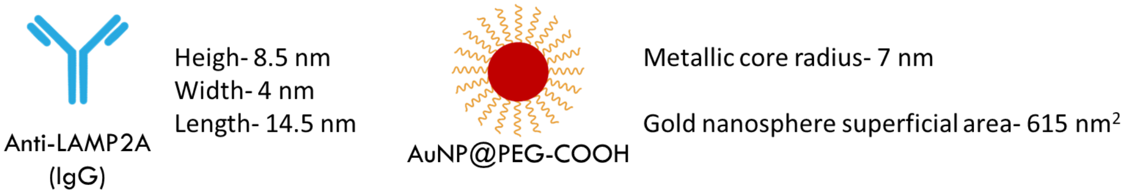

Taking into consideration the superficial area of the AuNP@PEG-COOH metallic core and only the width and length of an IgG, that is the superficial area that it will occupy, 58 nm^2, to fully cover the AuNP 10.6 antibody molecules are necessary.

Figure A2- *Calculation for maximum surface area coverage of a AuNP@PEG-COOH with an IgG (Anti-LAMP2A antibody [EPR4207(2)]-Lysosome Marker (ab125068))*

A.3 Bradford Assay

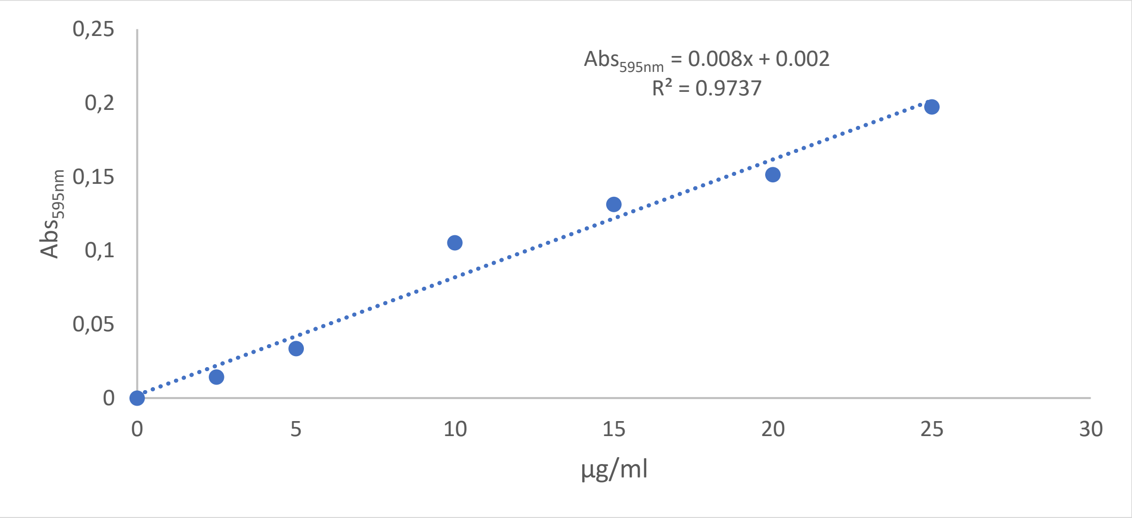

Figure A3- ***Bradford calibration curve.*** *Obtained through the absorbance reading at 595 nm of prepared bovine serum albumin (BSA) standard solutions ranging from 0-25µg/mL previously incubated with Coomassie reagent for 10 min, to calculate the concentration of excess antibody, removed after AuNP@PEG-COOH functionalization, and determine reaction yield.*

A.4 Determination of Citrate Capped AuNP Diameter

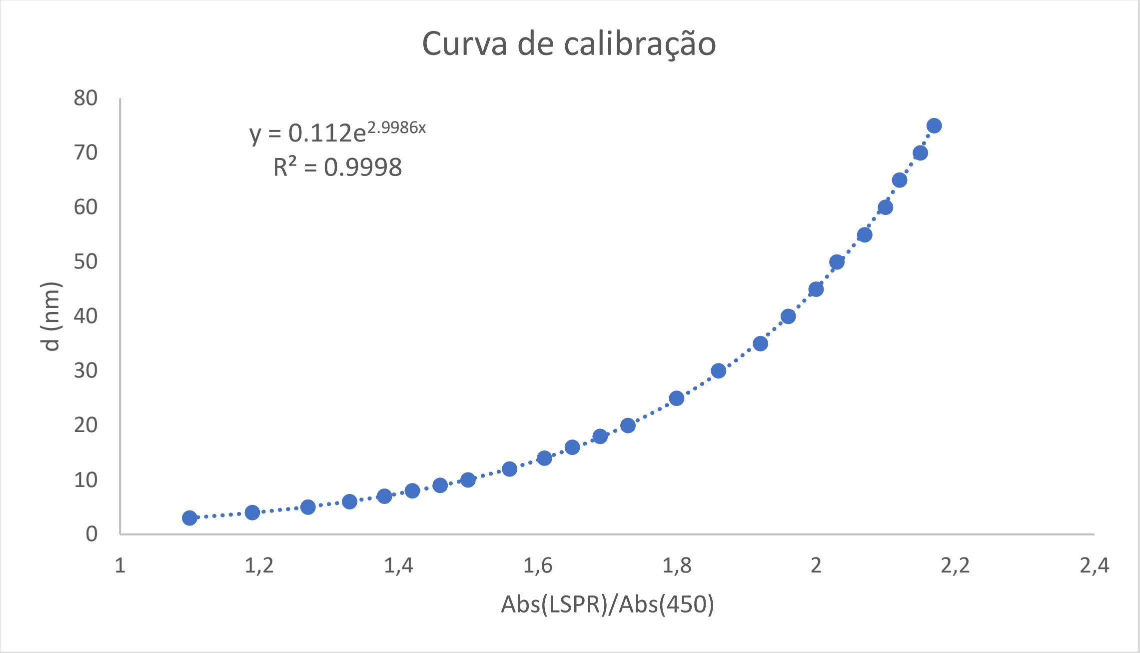

Figure A4- ***Calibration curve performed by Heiss et al.*** [98] *for the determination of citrate capped AuNP diameter using the absorbance values of the localized surface plasmon resonance (LSPR) peak and at 450nm.*

A.5 Pierce Assay

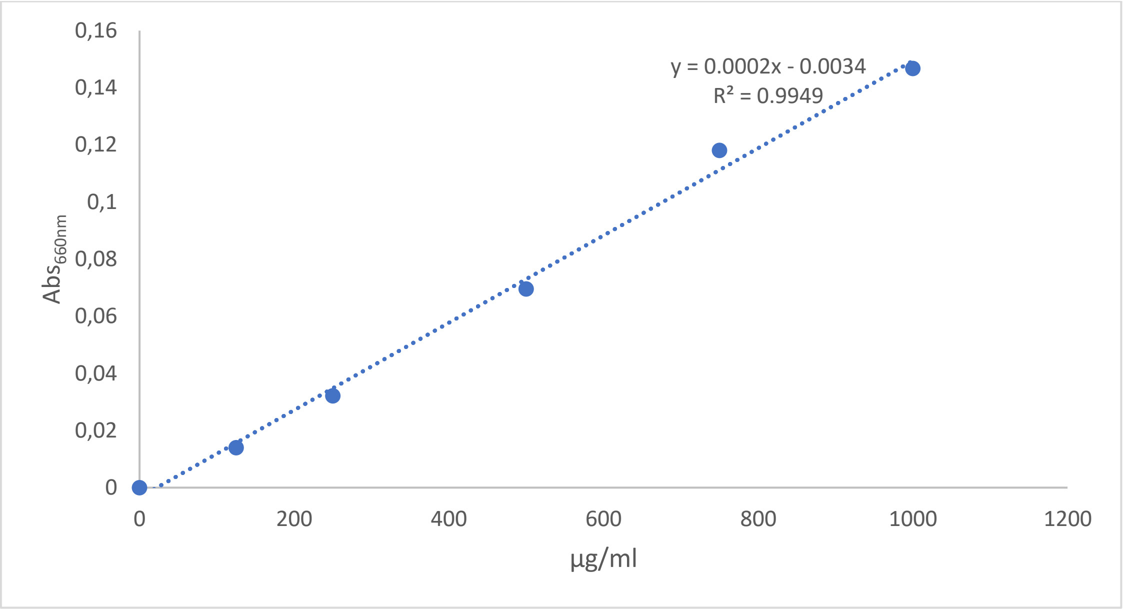

Figure A5- ***Pierce calibration curve.*** *Obtained through the absorbance reading at 660 nm of prepared bovine serum albumin (BSA) standard solutions ranging from 0-1000µg/mL previously incubated with Pierce reagent for 5 min, to calculate the protein concentration of the cellular fractions.*

A.6 Protein Transfer to the Nitrocellulose Membrane

Figure A6- ***Semi-dry transfer system representation.*** *Adapted from Abcam's General western protocol.*

B

ANNEX B

B.1 Photothermal Assay

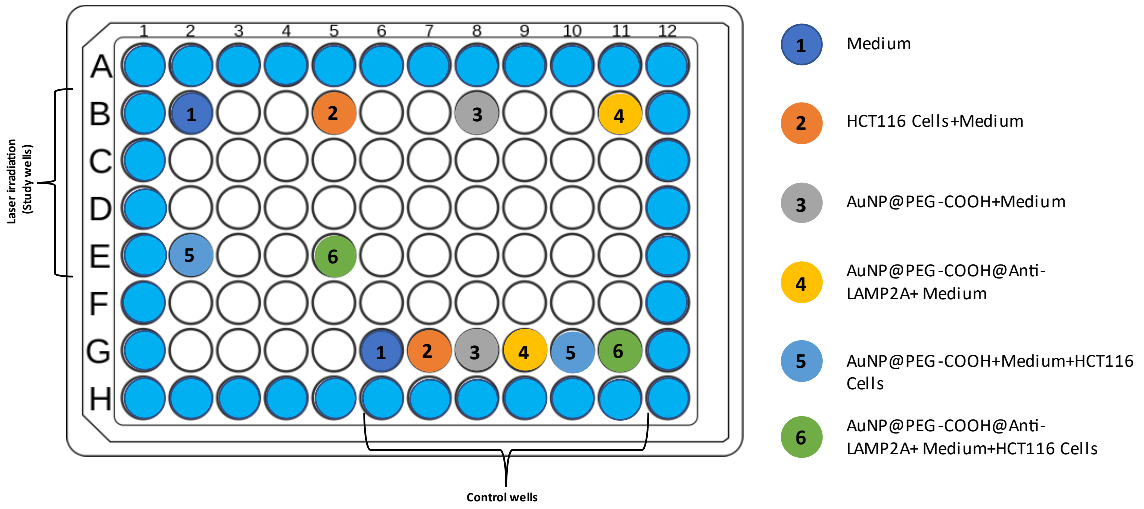

Figure B1- *Representation of the 96 well plate for photothermy.*

B.2 Immunofluorescence Microscopy

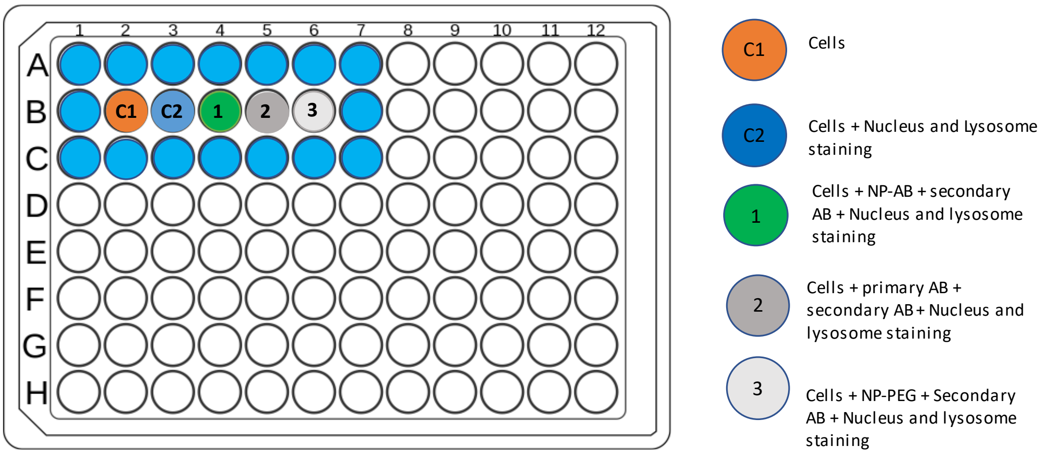

Figure B2- *Representation of the 96 well plate for Immunofluorescence Microscopy.*